UNDERDOPED CUPRATES: DETECTION OF CHARGE INHOMOGENEITY AND THE TRANSITION TO MAGNETIC ORDER

RINAT OFER

UNDERDOPED CUPRATES: DETECTION OF CHARGE INHOMOGENEITY AND THE TRANSITION TO MAGNETIC ORDER

RESEARCH THESIS

SUBMITTED IN PARTIAL FULFILLMENT OF THE
REQUIREMENTS
FOR THE DEGREE OF DOCTOR OF PHILOSOPHY

RINAT OFER

SUBMITTED TO THE SENATE OF THE TECHNION — ISRAEL INSTITUTE OF TECHNOLOGY
ELUL, 5768 HAIFA SEPTEMBER, 2008

THIS RESEARCH THESIS WAS SUPERVISED BY PROF. AMIT KEREN
UNDER THE AUSPICES OF THE PHYSICS DEPARTMENT

ACKNOWLEDGMENT

THE GENEROUS FINANCIAL HELP OF THE TECHNION AND THE ISRAEL SCIENCE FOUNDATION IS GRATEFULLY ACKNOWLEDGED

Contents

Abstract **xiv**

List of symbols **1**

1 Charge Inhomogeneity in YBCO Using NQR **3**

2 The experimental methods **7**

2.1 The YBCO Compound 7

2.1.1 Samples preparation 8

2.2 Nuclear Magnetic Resonance (NMR) 10

2.2.1 The quadrupolar term 11

2.2.2 FID and spin echo 13

2.3 Nuclear Quadruple Resonance (NQR) 15

2.3.1 The asymmetry parameter in YBCO 16

2.4 Nutation Spectroscopy 18

2.5 Angle dependent NQR (ADNQR) 21

2.5.1 The orientation of the EFG tensor 23

2.6 The experimental setup 24

3 Site assignment **28**

4 Results 32

4.1 NMR results 32

4.2 Nutation Spectroscopy results 34

4.3 ADNQR results 35

5 Discussion and Conclusions 39

6 Universal doping dependence of the ground state staggered magnetization in cuprates 42

7 The experimental methods 46

7.1 The CLBLCO System 46

7.1.1 Sample preparation 47

7.2 Neutron powder Diffraction 48

7.2.1 Rietvelt refinement 49

7.3 Muon Spin Rotation (μSR) 50

7.3.1 Muon production, implantation and decay 50

7.3.2 Experimental setup 51

7.3.3 Muons in matter in Zero Field 54

8 Summary of Our Previous μSR Results 57

9 Results 61

9.1 Neutron Diffraction results 61

9.2 μSR results 64

10 Discussion and Conclusions 72

A Derivation of the NQR Hamiltonian **75**

A.0.1 The EFG 76

A.0.2 The quadrupole tensor of the nucleus 76

A.0.3 Quantum mechanical treatment 77

B Interaction with an external time dependent magnetic field **80**

References **84**

Hebrew Abstract **ה**

List of Figures

1.1 STM measurement taken by [1]. These are real-space conductance maps at 100K, showing the appearance and energy evolution of density of states modulation along the Cu-O bond directions. 6

2.1 Phase diagram of YBCO$_y$ 7

2.3 Theoretical powder average NMR lines for spin 3/2 calculated from Eq. (2.7). 13

2.4 A schematic description of a spin echo sequence. The two pulses are followed by a Gaussian shaped echo. The schematic polarization graphs are for spins 1/2 in NMR 14

2.5 A toy model calculation for $|\eta|$ in the presence of charge strips in the CuO$_2$ plane. See text for details. 17

2.6 Calculated on-resonance nutation spectra for randomly oriented powder samples. The numbers are the η value. Taken form Ref. [2] 20

2.7 Basic Angle dependent NQR configuration. A sample with a preferred direction is inserted into the coil. The angle θ between them can be varied with a motor. 21

2.8 Theoretical echo intensity curves according to Eq.(2.29), for various values of η in an oriented powder, as a function of the polar angle θ between the RF field and the $\hat{z}$ direction of the EFG. 23
2.9 An illustration of a possible orientation on the EFG tensor with respect to the YBCO lattice. 25
2.10 The nutation spectroscopy prob. The coil goes through a current monitor that allows measurements in different frequencies with the same current. 26
2.11 Pulse sequence for the nutation spectroscopy NQR. 27
2.12 The ADNQR probe. 27

3.1 NQR frequency sweep on YBCO [3]. The dotted line is the experimental result. The solid line is a Gaussian fit performed in order to determine the resonance frequencies. 29
3.2 Schematic illustration of the Cu site with locally different oxygen coordinations. 30
3.3 T_c for different YBCO samples as a function of the NQR frequencies. The solid lines are fits of the data to three lines with shared slope ($dT_c/df = 37 \pm 4$[K/MHz]). 31

4.1 ^{63}Cu NMR spectra at 100K and 88MHz of different YBCO$_y$ samples. The satellites intensity is multiplied by a factor of 5. 33

4.2 (a) Cu NQR line shape for $YBCO_7$ with natural abundance of ^{65}Cu and ^{63}Cu. (b) and (c) Cu NQR line shape for $YBCO_{6.73}$ and $YBCO_{6.68}$ enriched with ^{63}Cu. The arrows show the frequencies where nutation spectroscopy is applied. (d)(e) and (f) nutation spectra for these three samples. 36
4.3 (a) Cu NQR line shape for $YBCO_7$ with natural abundance of ^{65}Cu and ^{63}Cu. (b) Cu NQR line shape for $YBCO_{6.68}$ enriched with ^{63}Cu. The arrows show the frequencies where ADNQR is applied. (c) and (d) The echo intensity as a function of the angle θ between the rf field and the principal axis of the EFG, for the two samples. The solid lines are fits to Eq. (2.29). 37

6.1 An illustration of The Cu-O plane in cuprates. On the left: The parent compound. The blue are the copper atoms and the red are the oxygen atoms. On the right: A simplified one band model of the electronic structure, with electrons hopping with hopping rate t. There is an AFM exchange J between spins on neighboring sites. 43
6.2 A Theoretical calculation of the doping dependence of the ground state staggard magnetization for different t/J, as calculated by Yamamoto *et al.* in Ref. [4]. 44

7.1 The $(Ca_xLa_{1-x})(Ba_{1.75-x}La_{0.25+x})Cu_3O_y$ (CLBLCO) unit cell. 47
7.2 The CLBLCO phase diagram including magnetic (close symbols) and superconducting (open symbols) critical temperatures. 48

7.3 A schematic diagram of the MuSR experiment. A muon, with its polarization aligned antiparallel to its momentum, is implanted in the sample. It then rotates about the local magnetic field B with the Larmor frequency, and decays to a positron preferentially along the direction of the muon's spin at the time of the decay. 53

7.4 On the Left: The number of positrons detected in the forward and backward detectors. On the right: The muon Asymmetry function. . 54

7.5 The muon spin precession about the magnetic field at an angle θ. . . 55

7.6 The Kubo-Toyabe polarization, the relaxation of the muon-spin due to a Gaussian field distribution. 56

8.1 The CLBLCO phase diagram after scaling: For each family (x), the critical temperatures are normalized by T_c at optimal doping, and y is replaced by Δp_m (see text for details). Inset: The normalized staggered magnetization as a function of the normalized temperature. The symbols are the experimental results, taken by measuring the oscillation frequency of the polarization curves. The solid lines are the theoretical curves plotted according to Eqs. 8.2 to 8.5. 58

8.2 The same as Fig.8.1 but the Néel temperature is corrected for anisotropy contribution so it is the same as J for the parent compound (see text). 59

9.1 Neutron powder diffraction data and refinement for a sample with x=0.1 and y=7.06. 62

9.2 The parameters extracted from a neutron diffraction experiment as a function of oxygen doping for the four families of CLBLCO. (a) The lattice parameter a. (b) The lattice parameter c. (c) θ - the buckling angle between the copper and oxygen in the plane. (d) R_{24} - The distance between the in-plane copper and the apical oxygen. The empty symbols are measurements taken from [5]. The lines are guides to the eye. 67

9.3 (a) The hopping rate t_{dd}, and (b) the superexchange coupling J calculated from Eq. (9.6) and (9.8), using the parameters shown in Fig. 9.2. (c) The ratio t_{dd}/J as a function of doping. The dotted lines are guides to the eye. All data sets are normalized to the $x = 0.1$ familiy. 68

9.4 Raw muon polarization data and fits to Eq. 9.9 for four samples from the $x = 0.4$ family 69

9.5 (a) The zero temperature muon oscillation frequency ω as a function of the chemical doping y for all four of the $(\mathrm{Ca}_x\mathrm{La}_{1-x})(\mathrm{Ba}_{1.75-x}\mathrm{La}_{0.25+x})\mathrm{Cu}_3\mathrm{O}_y$ (CLBLCO) families. The antiferromagnetic zero temperature order parameter M_0 is proportional to ω. (b) The CLBLCO phase diagram as shown in section 7.1 70

9.6 (a) The zero temperature muon oscillation frequency as a function of Δp_m for all four CLBLCO families; an equivalent to the staggered magnetization M_0 versus mobile hole density. The arrows show the expected variation of the critical doping from a 5% variation in t/J. (b) The CLBLCO phase diagram after scaling. as shown in chapter 8 71

Abstract

This work consists of two separate parts. In the first part we measure charge inhomogeneity in the CuO_2 planes of the cuprate compound $YBa_2Cu_3O_y$(YBCO) at different doping levels. One of the key challenges in the cuprates study is to determine whether the charge inhomogeneity found in some of these compound, is an essential part of the mechanism of superconductivity. Bulk measurements of the plane anisotropy for YBCO have been done so far only for the optimally doped compound. Our objective in this part is to detect possible charge inhomogeneity in underdoped YBCO, and see if there is a correlation between the electronic structure of the CuO_2 planes and the dopant atoms. This will alow us to tell if models that predict inhomogeneity without taking into account the dopant, are relevant to high temperature superconductors (HTSC) or not.

For this purpose we perform Nuclear Magnetic Resonance (NMR) and Quadrupole Magnetic Resonance (NQR) measurements, on fully ^{63}Cu enriched YBCO. We compare a new method, called Angel Dependent NQR (ADNQR), with the nutation spectroscopy NQR and the conventional NMR. We show that the ADNQR is more sensitive to the inhomogeneity. Finally, we conclude that any charge inhomogeneity in the CuO_2 planes is found only in conjunction with oxygen deficiency in the chains. In other words, if there is a phase separation in the planes in the YBCO compound, it is correlated with the O dopant atoms.

Upon further underdoping of cuprates they lose their inhomogeneity and become magnetically ordered. In the second part of this thesis we use muon spin rotation to determine the zero temperature staggered antiferromagnetic order parameter M_0 versus hole doping measured from optimum Δp_m, in the $(\mathrm{Ca}_x\mathrm{La}_{1-x})(\mathrm{Ba}_{1.75-x}\mathrm{La}_{0.25+x})\mathrm{Cu}_3\mathrm{O}_y$ system. In this system the maximum T_c and the superexchange J vary by 30% between families (x). $M_0(x, \Delta p_m)$ is found to be x-independent. Using neutron diffraction we also determine the lattice parameters variations for all x and doping, and estimate the hopping rate t and the superexchange J from simple structure considerations.

We show that the origin of the different energy scales between the CLBLCO families is mainly the different in-plane buckling angles. The comparison between the t/J ratio extracted from the neutron measurements and the doping dependence of the order parameter, suggests that at zero temperature for this compound the order parameter as a function of mobile holes is independent of t/J.

We offer two possible explanation for our results. One is that at low temperatures the effective Hamiltonian is given by a t-J model but with an effective t that is proportional to J. The second is that the destruction of the AFM order parameter is not a result of single holes hopping and should be described by a completely different Hamiltonian, perhaps hopping of boson pairs.

List of symbols

T_C	Superconducting transition temperature
Cu(1)	Cupper in the CuO_2 planes
Cu(2)	Cupper in the Cu-O chains
NMR	Nuclear Magnetic Resonance
NQR	Nuclear Quadrupole Resonance
μ	Magnetic moment of the nucleus
I	Spin of the nucleus
H_0	Static magnetic field
γ	Gyromagnetic ratio
E	Energy
B_1	Amplitude of the alternating magnetic field
ω	rf transmission frequency
V	Electric Potential
EFG	Electric Field Gradient
V_{ij}	Electric Field Gradient Tensor
ν_q	A frequency scale, determined by the main component of the EFG
η	The asymmetry parameter
Q	Quadruple moment of the nucleus

θ,ϕ	Polar angels between the rf field and the main components of the EFG
t_p	duration of the rf pulse
FID	Free Induction Decay
t	Time measured from the end of the pulse
τ	Time between pulses
f_{NQR}	NQR frequency
ω_p	the nutation experiment frequency
ADNQR	Angle dependent Nuclear Quadruple Resonance
$M(\eta,\theta,\phi)$	The magnetization in the coil
t	Hopping rate
U	Repulsive energy cost due to screened Coulomb interaction
J	The Heisenberg superexchange
AFM	Antiferromagnet
M_0	Staggered antiferromagnetic order parameter
T_N	Neel Temperature
T_g	Spinglass transition temperature
μSR	Muon Spin Rotation
$A(t)$	Moun asymmetry
Δp_m	mobile hole parameter measured from optimum

Chapter 1

Charge Inhomogeneity in YBCO Using NQR

The parent compounds of the cuprates superconductors are antiferromagnetic insulators. Hole doping the CuO_2 planes destroys the long range antiferromagnetism. Above a certain doping level, superconductivity emerges. This doping creates natural inhomogeneity.

In the first part of this thesis we use nuclear magnetic resonance (NMR) and nuclear quadrupole resonance (NQR) in order to measure charge inhomogeneity in the CuO_2 plane of the $YBa_2Cu_3O_y$(YBCO) compound. We compare three different techniques to measure this inhomogeneity. The question of the origin of the charge inhomogeneity seen in some of the cuprates is a very basic one in our understanding of these compounds.

One of the main questions in this field is whether charge and spin inhomogeneity in the CuO_2 planes are essential to the mechanism of superconductivity in cuprates. For some of these materials, there is evidence for a phase separation with segregated hole-rich and hole-poor regions. It has been suggested that this phase separation, possibly in the form of strips, explains the unusual properties of the cuprates and leads to the superconductivity. There are several theoretical work (For examples see ref. [6][7][8][9][10][11]), that try to show that the phase separation is a characteristic of the Hubbard model, and therefore an intrinsic property of the CuO planes.

According to the model by Emery and Kivelson [12], the first stage in the cooling process is the formation of charge inhomogeneity in the form of strips at a temperature T_0. The segregation of holes leaves the rest of the system as an antiferromagnetic background. This phase separation results in the opening of the pseudo gap. Further cooling results in the formation of local spin pairs, that hop in and out the stripes to the magnetic background, creating a spin gap at a temperature T*. Finally at T_c there is an establishment of phase coherence between the pairs.

Indeed, inhomogeneity was found in $La_{2-x}Sr_xCu_1O_4$ (LSCO) by several methods. Nuclear Quadruple Resonance (NQR) measurements show that there is a distribution of T_1 (nuclear spin-lattice relaxation rate) in the spectrum that can be attributed to a spatial variation of the hole concentration [13]. Phase separation in LSCO was also found with neutron scattering [14] and muon spin relaxation (μSR) [15],[16].

In Addition, STM experiments on underdoped $Bi_2Sr_2CaCu_2O_y$ (Bi-2212) showed local density of states modulations [17] and inhomogeneity of the superconducting gap on the samples' surface, that can be associated with the distribution of holes in the planes [18],[19],[1]. An example of a picture taken with STM by M. Vershinin *et al.* [1] is presented in Fig. 1.1. This picture shows the spatial dependence of the density of state at different energies at 100K, indicating spatial modulation in the electronic excitations (with energies below the pseudogap energy).

In $YBCO_y$, phase separation was found at very low doping levels, up to $YBCO_{6.35}$, with neutron scattering from phonons related to charge inhomogeneity [20]. μSR measurements show the existence of a spin glass phase for a similar doping range [21][22]. ^{89}Y NMR study in YBCO$_y$ for $y = 7$ and $y = 6.6$ showed no phase separation at all [23]. The highest doping in which magnetic order was found in YBCO was in YBCO$_{6.6}$ [24] using neutron scattering.

In light of the above, our main question can be divided into the following subitems:

- Is charge inhomogeneity a necessary phenomenon for HTSC? If it is, then it should exist in all HTSC compound, including YBCO$_y$, which is considered by many, the cleanest system since the dopant has a natural place to go into.
- Does it exist only on the surface, or can it be detected in the bulk as well?

Clear detection of charge inhomogeneity in YBCO$_y$ is nearly impossible, since STM measurements are very difficult due to oxygen loss in vacuum and surface problems. Different STM experiments in this compound showed an inhomogeneous [25] or relatively homogenous surface [26], depending on the surface preparation procedure.

However, an NQR experiment is sensitive to the charge distribution in the bulk and not just on the surface, like an STM experiment. We perform NQR measurements on the Cu nuclei, since we are interested in the charge distribution in the Cu-O planes. The YBCO compound has narrow NQR resonance lines, which allow us to distinguish between different Cu(2) resonance lines, and associate each line with a local environment.

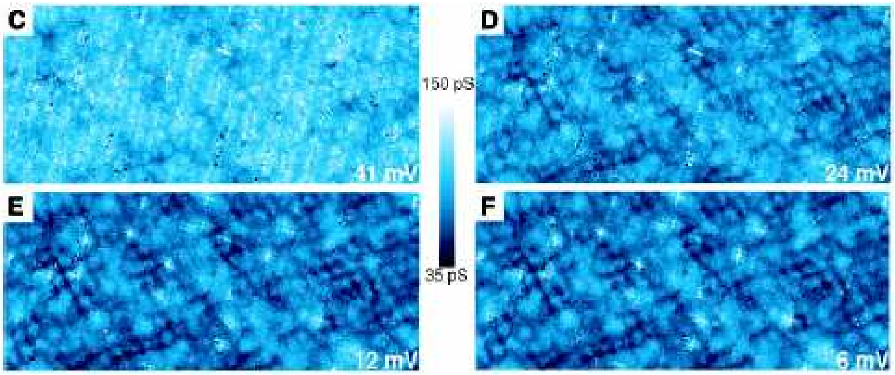

Figure 1.1: STM measurement taken by [1]. These are real-space conductance maps at 100K, showing the appearance and energy evolution of density of states modulation along the Cu-O bond directions.

Chapter 2

The experimental methods

2.1 The YBCO Compound

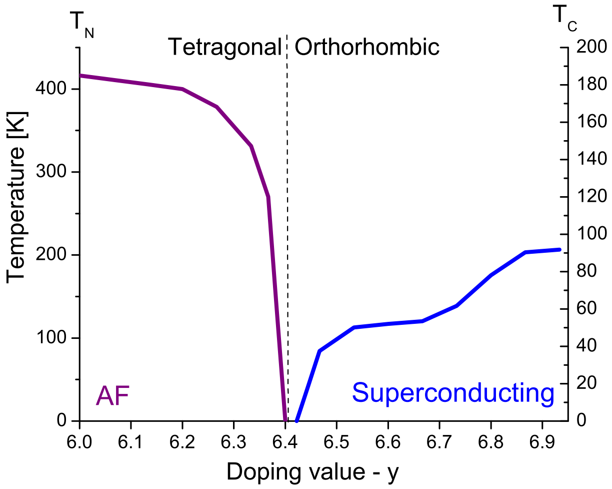

Figure 2.1: Phase diagram of $YBCO_y$

In this part we chose to work with the high temperature superconductor (HTSC) compound $YBa_2Cu_3O_y$ ($YBCO_y$). The phase diagram of this compound is shown

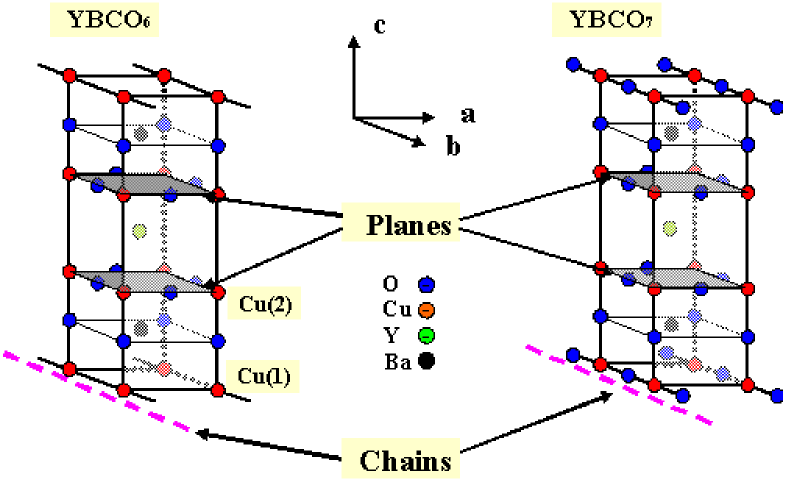

Figure 2.2

in Fig.2.1. At low temperatures it is tetragonal for $y < 6.4$, and orthorhombic for $y > 6.4$. The ($YBCO_y$) unit cell is shown in Fig. 2.2.

Apart from the CuO_2 planes, there are also one dimensional Cu-O chains. The copper in the chains is termed Cu(1) and the copper in the planes Cu(2). In $YBCO_6$ there are no Cu-O chains, and the compound is an antiferromagnetic insulator, as shown by neutron scattering experiments [27]. Doping is achieved by inserting additional oxygen atoms, which form the Cu-O chains. At an oxygen content of 6.4, antiferromagnetic long range order disappears and the superconducting phase starts developing.

2.1.1 Samples preparation

The samples are prepared by solid state reaction. Raw powders are machine milled and baked in air at 950 °C for one day and re-grounded repeatedly 3 times. Then the powder is pressed into pellets, and the pellets are sintered for 70h in flowing oxygen at 960 °C, and cooled at a rate of 10 °/h. The different oxygen content is achieved by reduction in a tube furnace in flowing oxygen at the right temperature. The reduction temperature determines the oxygen doping level in the material. After 24h in the furnace the samples are quenched in liquid N_2. The very underdoped samples ($y < 6.6$) are quenched in liquid Ar. The reason for that is that the liquid N_2 is not pure and contains O_2 molecules. At low doping levels there is a greater chance that these molecules will penetrate the sample during the quenching. This causes the samples to become oxygen inhomogeneous and the transition to superconductivity wider [28]. The oxygen content is measured by iodometric titration; this method is capable of measuring y with an error of ± 0.01.

Enriched samples

Previous Cu NQR measurements on YBCO (see Ref.[29],[30],[31],[32]) were performed on samples containing both Cu isotopes, Cu^{63} and Cu^{65}, so the frequency lines consisted of doublets of Cu^{63}-Cu^{65}. In this work, for a clearer understanding of the NQR signals, the YBCO samples were all made of enriched copper, meaning that these samples contained only the Cu^{63} isotope. This allows us to distinguish between the different contributions to the NQR line from different local environments.

Orientation

The ADNQR technique requires oriented samples. In the orientation process about 1gr of powder, mixed with StayCast glue, is inserted into a Teflon cylinder 1.2cm in length and 0.5cm in diameter. The sample is then inserted into a magnetic field of 8T, and shaken for 30 minutes at room temperature. The shaking is done by connecting it to an electromagnetic relay with a voltage of 10V and 25Hz square wave. The susceptibility of each grain in the powder, which is assumed to be a single crystal, creates the maximum magnetic moment in the direction of the crystal c axis. Hence, the orientation process aligns the YBCO grains so that all the (00l) planes are perpendicular to the magnetic field. After the orientation we identify the $\hat{z}$ direction of the YBCO crystal with the magnetic field direction.

2.2 Nuclear Magnetic Resonance (NMR)

In a NMR experiment a nucleus with spin I is immersed in a static magnetic field H_0, and exposed to a second oscillating magnetic field that causes transitions between the nuclear energy levels.

The energy of a single nucleus with magnetic moment μ in the presence of a magnetic field $H = H_0\hat{z}$ is:

$$\mathcal{H}_z = -\mu \cdot H = -\gamma\hbar I \cdot H = -\gamma\hbar H_0 I_z, \tag{2.1}$$

where γ is the gyromagnetic ratio of the nucleus. This Hamiltonian, describing the Zeeman interaction, has very simple eigenvalues:

$$E = -\gamma\hbar H_0 m \qquad m = I, I-1, ..., -I \tag{2.2}$$

In a resonance experiment, transitions between the energy levels are forced by applying an oscillating magnetic field perpendicular to the static field. This adds a time dependent perturbation term to the Hamiltonian of the form:

$$\mathcal{H}_{\mathcal{RF}} = \gamma\hbar B_x I_x \sin\omega t \tag{2.3}$$

where $\omega = 2\pi f$, f is the transmission frequency ,B_x is the amplitude of the alternating field. The operator I_x has matrix elements between states m and m' that vanishes unless $m' = m \pm 1$. Hence this term will cause transitions between levels adjacent in energy when

$$\hbar\omega = \Delta E = \gamma\hbar H_0 \tag{2.4}$$

or

$$\omega = \gamma H_0 \tag{2.5}$$

This resonance condition is met when the nucleus is entirely isolated from its surroundings. A nucleus in solid experiences several interactions, and other terms should be added to the Hamiltonian. The magnetic interaction between the nucleus and the surrounding electrons adds terms of the form: $\sigma\gamma\hbar H_0 I_z$, where σ is the magnetic shift tensors. These shifts can be Knight shifts (for metallic samples), chemical shifts (for diamagnetic samples) or paramagnetic shifts (for paramagnetic samples). Other possible terms are from dipolar interactions and the quadrupolar term which will be discussed next. The amount of shift will generally depend on the orientation of the nuclear environment relative to the applied field. For a single crystal, the resonance condition depends on the polar angles θ and ϕ, between the crystal axes and H_0. For a powder this condition should be averaged over all possible orientations, and the result is a powder pattern.

2.2.1 The quadrupolar term

Nuclei with spin greater then 1/2 have an electric quadrupolar moment, for these nuclei a quadrupolar term is added to the Hamiltonian. The origin of this term is the electrostatic interaction between the charge distribution of the nucleus and the potential V of the surrounding charges. These nuclei can be viewed as positively charged oval objects. Different orientations of the nucleus with respect to the surrounding charges will result in different energy levels. The energy difference between one configuration and another is determined by the Electric Field Gradient Tensor (EFG): $V_{ij} = \frac{\partial^2 V}{\partial x_i \partial x_j}$.

The axis directions of the EFG tensor can be chosen so that the tensor is diagonal; these directions are called the principal axis of the EFG. Due to the Laplace equation ($V_{xx} + V_{yy} + V_{zz} = 0$), the three parameters of the EFG can be replaced by only two parameters, ν_q and η. The quadrupolar term of the Hamiltonian can be written as [33]:

$$\mathcal{H}_Q = \frac{\hbar \nu_q}{6}[3I_z^2 - I^2 + \eta(I_x^2 - I_y^2)] \tag{2.6}$$

where:

I_α are the nucleus spin operators; ν_q is a frequency scale, determined by the EFG component V_{zz}, and the quadruple moment of the nucleus Q; $\eta = \frac{V_{xx}-V_{yy}}{V_{zz}}$ is the asymmetry parameter with the convention $|V_{zz}| \geq |V_{yy}| \geq |V_{xx}|$, and therefore $0 \leq \eta \leq 1$. In the case of axial symmetry, $\eta = 0$. (See appendix A for the full deviation of the quadrupolar Hamiltonian).

In the case of strong H_0 the quadrupolar term can be treated as a perturbation to the Zeeman Hamiltonian. In first-order perturbation theory the NMR transitions consists of unshifted central resonance, and $2I - 1$ "satellite" lines. When the quadrupolar effect is large enough to require second-order perturbation theory, the central line is also shifted, as well as the satellites [34].

To the first order in perturbation theory the NMR transitions resulting from the Zeeman and quadrupolar terms only (neglecting other shifts) are:

$$\nu_{m \leftrightarrow m-1} = \gamma H_0 - \nu_q[\frac{1}{2}(3\cos^2\theta - 1) - \frac{1}{2}\eta \sin^2\theta \cos 2\phi](m - \frac{1}{2}). \tag{2.7}$$

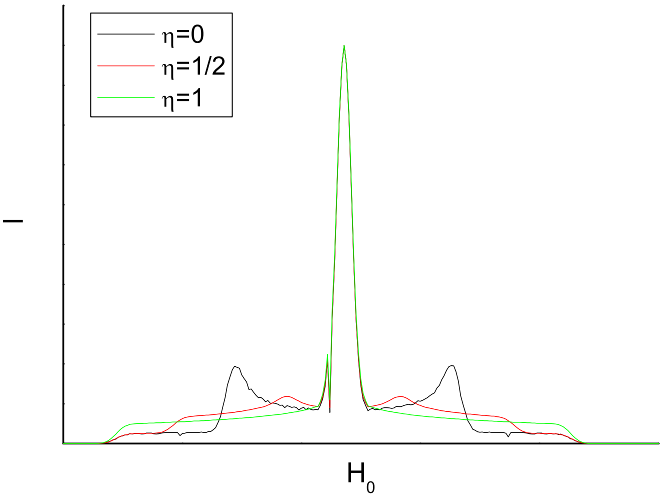

Figure 2.3: Theoretical powder average NMR lines for spin 3/2 calculated from Eq. (2.7).

For a spin 3/2 nuclei, The NMR line consists of 1 central line and 2 satellites. Fig. 2.3 show a theoretical NMR line for spin 3/2 in a powder for different values of η, calculated from Eq. (2.7). For $\eta = 0$ there are two clear satellites, however for larger η it becomes more difficult to determine the location of the satellites. In this work we measure partially oriented powder for which this result is not exact. But still it shows the general trends.

2.2.2 FID and spin echo

Before the RF pulse is applied, the static field induces a net polarization in the $\hat{z}$ direction. Applying the RF pulse leads, after some time, to a net magnetization in the $\hat{x}$ direction. When the pulse ends the spins start to rotate about the direction of

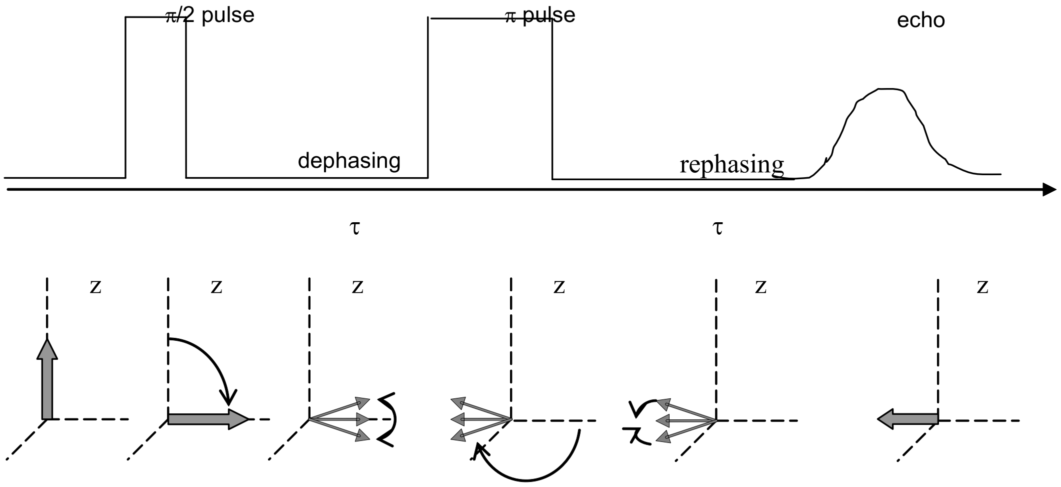
π/2 pulse
π pulse
echo
dephasing
rephasing
τ
τ
z
z
z
z
z
z

Figure 2.4: A schematic description of a spin echo sequence. The two pulses are followed by a Gaussian shaped echo. The schematic polarization graphs are for spins 1/2 in NMR

the static field. The voltage induced in the coil after the pulse will be [35]:

$$V \propto \sin(\sqrt{3}\gamma B_x t_p)\cos\omega t, \tag{2.8}$$

where t_p is the duration of the pulse and t is the time measured from the end of the pulse. Due to relaxation effects the magnitude of the polarization vector will decay with time. The decaying signal is called Free Induction Decay (FID). The main shortcoming with FID is that the signal appears immediately after the pulse. Due to the intensity of the pulse the electronics in the experiment is usually very noisy after the pulse, and the FID signal in mixed with this noise. This problem is solved by the spin echo $\pi/2-\tau-\pi$ sequence.

A $\pi/2$ pulse is a pulse with length $t_{\pi/2}$, during which the net polarization rotates from the $\hat{z}$ direction to the x-y plane. When the pulse ends the spins start to rotate in the x-y plane and begin to dephase. After a time τ a second pulse (called the refocusing pulse) with length $2t_{\pi/2}$ is applied. This pulse rotates the magnetization by 180^o about the $\hat{x}$ axis back to the x-y plane. The pulse causes the magnetization to rephase and produce a signal called an echo after a time τ from the second pulse. A schematic description of a spin echo sequence in NMR is shown in Fig. 2.4.

2.3 Nuclear Quadruple Resonance (NQR)

In a pure NQR experiment there is no permanent magnetic field H_0, and the hamiltonian consists of only the quadrupolar term shown in Eq. (2.6). For the spin 3/2 copper nucleus, the quadrupolar Hamiltonian has two energy levels (one for spin ±1/2 and the other for spin ±3/2), and therefore only one resonance frequency, given by:

$$f_{NQR} = \hbar\nu_q\sqrt{1+\frac{\eta^2}{3}}. \tag{2.9}$$

(see appendix A for more details).

An NQR experiment on a nuclear spin 3/2 is very similar to a NMR experiment on a nuclear spin 1/2. However, in NQR on spin 3/2 the situation is slightly more complicated. Since for the NQR Hamiltonian there are two energy levels, one for spin $\pm 1/2$ and the other is for spin $\pm 3/2$, there is no net polarization in the $\hat{z}$ direction. A spin echo sequence in an NQR experiment is based on the fact that for a spin 3/2 nucleus, the energy levels can be viewed as two sets of a two level system. The first set, with $s_z = 3/2$ and $s_z = 1/2$, can be viewed as a spin I_1 in a field H_0 (so the total spin is pointing in the $\hat{z}$ direction); a second set with $s_z = -3/2$ and $s_z = -1/2$ can be viewed as spin I_2 in a field $-H_0$ (so the total spin is pointing in the $-\hat{z}$ direction). The $\pi/2$ pulse rotates the spins about the $\hat{x}$ axis to the $x-y$ plane; the spins are now in the $\hat{y}$ and $-\hat{y}$ direction respectively, and there is still no net magnetization. After the pulse, I_1 and I_2 are rotating in opposite directions (according to H_0 and $-H_0$), and a magnetization is obtained in the $\hat{x}$ direction. The spins rotate in this plane and begin to dephase. After a time τ the refocusing pulse is applied and rotates the spins by 180^o about the $\hat{x}$ axis back to the $x-y$ plane. This causes the magnetization to at least partially rephase and to produce an echo.

2.3.1 The asymmetry parameter in YBCO

In this work we measure the YBCO$_y$ compound (see section 2.1). For the copper in the CuO$_2$ plane in YBCO$_7$ and YBCO$_6$, the EFG principle axis are known experimentally [36][37]: $\hat{z}$ is the $\hat{c}$ direction and $\hat{x}$ and $\hat{y}$ are directions in the CuO$_2$ plane. Assuming that the directions are doping independent, ν_q is an indication of the site the nuclear sits in, and η is a measure of charge isotropy of the CuO$_2$ plans. When these planes are homogeneous with local xy rotation symmetry, $\eta = 0$. In contrast, when the

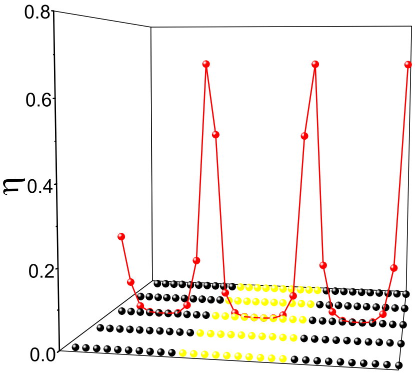

Figure 2.5: A toy model calculation for $|\eta|$ in the presence of charge strips in the CuO_2 plane. See text for details.

planes are inhomogeneous, duo to phase separation as in the case of strips, the xy symmetry is lost on the boundary between the hole-poor and hole-rich strips, and we expect $\eta \neq 0$. This situation is demonstrated, for simplicity, in Fig. 2.5 obtained using a toy model. In this model, a plane of a square lattice with total charge Q is sandwiched between two similar planes with total charge $-Q/2$ each. The electric field of each ion is screened with a screening length of two lattice sites. The figure shows only the central plane. The charge in this plane is distributed in a form of strips, and η is calculated numerically from Eq. (2.29) and shown along one line of ions. This figure demonstrates that as a result of the strips $\eta \neq 0$ for all nuclei on the boundary between strips, though the lattice is square.

In the standard NQR experiment, η and ν_q from Eq.(2.9), cannot be separately determined. In the following sections we review two methods that use NQR measurements in order to determine η and ν_q.

2.4 Nutation Spectroscopy

The nutation spectroscopy NQR is a method in which the signals are measured as a function of the duration of the rf excitation pulse [38][39]. This method is used to determine the asymmetry parameter η.

To explain this method we start with a single nucleus with axially symmetric quadrupolar axis ($\eta = 0$), in zero static magnetic field, under on-resonance rf pulse. For the rf magnetic field H_1 we define the rotating frame frequency $\omega_1 = \gamma H_1$. The strength of H_1 in a frame rotating about the EFG axis at the quadrupolar frequency, depends on the angle θ between the coil and the EFG. The nutation frequency is given by:

$$\omega_N = \sqrt{3}\omega_1 \sin(\theta/2) \tag{2.10}$$

The voltage induced in the coil by the precessing magnetization following the rf pulse is also proportional to $\sin\theta$.

After an FID pulse of duration t_p, the signal intensity after a time t is given by:

$$I(t_p, t, \theta) \propto \sin\theta \sin(\omega_N t_p) \sin(\omega_Q t) = \sin\theta \sin(\sqrt{3}\sin(\theta/2)\omega_1 t_p) \sin(\omega_Q t) \tag{2.11}$$

where $\omega_Q = e^2qQ/2h$ is the quadrupolar frequency in the case of $\eta = 0$.

From Eq. (2.9), when the nucleus quadrupolar axis are not axially symmetric, the quadrupolar frequency is given by

$$\omega_Q = \frac{e^2qQ}{2h}\sqrt{1 + \frac{\eta^2}{3}} \tag{2.12}$$

Pratt *et al.*[40] showed that in this case the angular factor should be replaced by a factor:

$$\lambda(\theta, \phi) = \sqrt{r_x^2 a_x^2 + r_y^2 a_y^2 + r_z^2 a_z^2} \tag{2.13}$$

$$a = (\eta + 3, \eta - 3, 2\eta) \tag{2.14}$$

and the symmetry axis of the coil with respect to the principal axis of the EFG is:

$$r = (\sin\theta\cos\phi, \sin\theta\sin\phi, \cos\theta) \tag{2.15}$$

θ and ϕ are the polar angles relating the coil axis to the quadrupolar frame. Hence,

$$\lambda(\theta, \phi) = \sqrt{(9 + \eta^2 + 6\eta\cos(2\phi))\sin^2\theta + 4\eta^2\cos^2\theta} \tag{2.16}$$

The signal in this case is:

$$I(t_p, t, \theta, \phi, \eta) \propto \lambda(\theta, \phi)\sin(\frac{\lambda(\theta, \phi)}{2\sqrt{3 + \eta^2}}\omega_1 t_p)\sin(\omega_Q t) \tag{2.17}$$

Integrating over the frequencies for isotropic powder gives:

$$I(t_p, t, \eta) \propto \int_0^{2\pi} d\phi \int_0^{\pi} \sin\theta d\theta\lambda(\theta, \phi)\sin(\frac{\lambda(\theta, \phi)}{2\sqrt{3 + \eta^2}}\omega_1 t_p)\sin(\omega_Q t) \tag{2.18}$$

The fourier transform on t_p gives a powder pattern line shape that is described by:

$$I(w_p, t, \eta) \propto \int_0^{2\pi} d\phi \int_0^{\pi} \sin\theta d\theta\lambda(\theta, \phi) \int_{-\infty}^{\infty} e^{i\omega_p t_p} dt_p \sin(\frac{\lambda(\theta, \phi)}{2\sqrt{3 + \eta^2}}\omega_1 t_p)\sin(\omega_Q t) \tag{2.19}$$

Fig. 2.6 shows the powder patterns for different values of η.

The fourier transform over t_p gives a delta function with the frequency:

$$\omega_p(\theta, \phi) = \frac{\lambda(\theta, \phi)}{2\sqrt{3 + \eta^2}}\omega_1 \tag{2.20}$$

Differentiating (2.20) with respect to θ and ϕ gives 3 singularities:

$$\theta = 0 \qquad \omega_I = \frac{2\eta}{2\sqrt{3 + \eta^2}}\omega_1 \tag{2.21}$$

$$\theta = \pi/2 \qquad \phi = 0 \qquad \omega_{II} = \frac{\eta + 3}{2\sqrt{3 + \eta^2}}\omega_1 \tag{2.22}$$

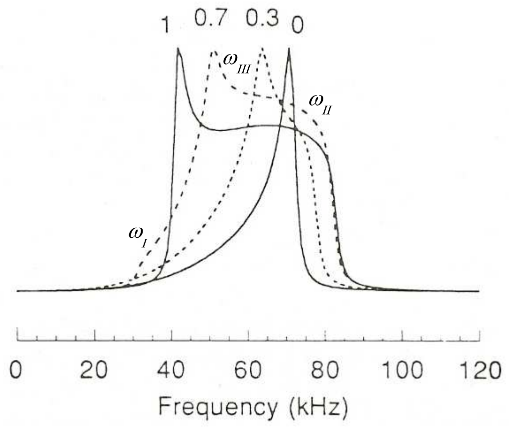

Figure 2.6: Calculated on-resonance nutation spectra for randomly oriented powder samples. The numbers are the η value. Taken form Ref. [2]

$$\theta = \pi/2 \qquad \phi = \pi/2 \qquad \omega_{III} = \frac{\eta - 3}{2\sqrt{3+\eta^2}}\omega_1 \tag{2.23}$$

These singularities can be seen in Fig. 2.6 next to the $\eta = 0.7$ line. At $\eta = 0$, $\omega_{II} = \omega_{III}$ and $\omega_I = 0$, therefore there is one sharp frequency. As η grows there is a separation to the 3 singularities. From these singularities η can be extracted: $\eta = \frac{\omega_{III} - \omega_{II}}{\omega_{III} + \omega_{II}}$

For a spin echo sequence, after a time τ from the first pulse there is a refocusing pulse with duration t_r. The nutation line shape now becomes:

$$I(w_p, t, \eta) \propto \int_0^{2\pi} d\phi \int_0^{\pi} \sin\theta d\theta \lambda(\theta,\phi) \int_{-\infty}^{\infty} e^{i\omega_p t_p} dt_p \sin(\frac{\lambda(\theta,\phi)}{2\sqrt{3+\eta^2}}\omega_1 t_p) \sin^2(\frac{\lambda(\theta,\phi)}{\sqrt{3+\eta^2}}\omega_1 t_r) \sin(\omega_Q t) \tag{2.24}$$

In an NQR experiment, since the spin rotation frequency depends on the orientation of the lattice with respect to the coil, the second pulse can not perfectly refocus all the magnetization. The additional factor $\sin^2(\frac{\lambda(\theta,\phi)}{\sqrt{3+\eta^2}}\omega_1 t_r)$ does not change the nutation frequencies $\omega_{I,II,III}$ from the FID case, however it does change the relative intensities of these frequencies with respect to each other. The general shapes are shown in Fig. 2.6.

The main advantage of this method is that it is relatively simple to execute, it can be carried out on a simple NQR spectrometer without a static magnetic field or additional modifications. This method can be preformed on powders. It allows the determination of η at every point of the NQR spectrum (unlike NMR, where η can be determined only from the entire spectrum with no local resolution).

2.5 Angle dependent NQR (ADNQR)

The angle dependent NQR technique on an oriented powder, was recently developed by Levi and Keren [41]. In this technique the signal intensity for a given frequency is measured as a function of θ, the angle between the direction of the rf field and the component V_{zz} of the EFG. In the experiment the sample is rotated with respect to the symmetry axis of the coil (see Fig.2.7).

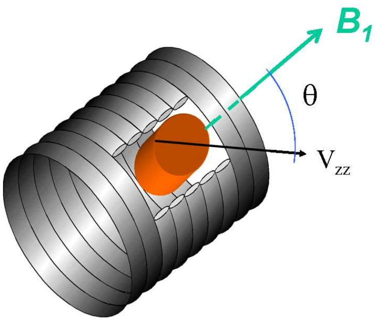

Figure 2.7: Basic Angle dependent NQR configuration. A sample with a preferred direction is inserted into the coil. The angle θ between them can be varied with a motor.

The NQR Hamiltonian is (see section 2.2.1):

$$\mathcal{H}_Q = \frac{\hbar\nu_q}{6}[3I_z^2 - I^2 + \eta(I_x^2 - I_y^2)] \tag{2.25}$$

The rf pulse Hamiltonian is (see section 2.2):

$$\mathcal{H}_{rf} = \gamma\hbar\mathbf{B}_1 \cdot I \sin\omega t \tag{2.26}$$

In general, the rf field can be described as:

$$\mathbf{B}_1 = 2H_1\left[\sin(\theta)\cos(\phi), \sin(\theta)\sin(\phi), \cos(\theta)\right] \tag{2.27}$$

For $\eta = 0$, $\mathcal{H}_Q$ and $\mathcal{H}_{rf}$ commute when $\theta = 0$. In this case there will be no spin transitions and no signal. For $\eta > 0$, $\mathcal{H}_Q$ and $\mathcal{H}_{rf}$ do not commute even for $\theta = 0$. In this case we expect a signal even when $\mathbf{B}_1$ is in the $\hat{z}$ direction.

Levi and Keren showed [41] that for a $\pi/2-\tau-\pi$ pulse sequence the magnetization in the coil at the time of the echo is given by:

$$M(\eta,\theta,\phi) = \frac{\lambda(\theta,\phi)\omega}{4\sqrt{3}KT}\sin^3\left(\frac{\lambda(\theta,\phi)\omega_1 t_{\pi/2}}{2\sqrt{3}}\right) \tag{2.28}$$

where: $\omega_1 = \gamma B_1$; $t_{\pi/2}$ is the duration of the $\pi/2$ pulse; $\lambda(\theta,\phi)$ is the same as in Eq. (2.16); and θ and ϕ are the angles between the EFG axis and B_1.

In the case of an oriented powder (if we assume V_{zz} is in the $\hat{c}$ direction), the $\hat{a}$ and $\hat{b}$ directions are mixed and M is obtained by averaging over ϕ, namely:

$$M(\eta,\theta) = \frac{1}{2\pi}\int_0^{2\pi} M(\eta,\theta,\phi)d\phi \tag{2.29}$$

Theoretical echo intensity curves as a function of θ for various values of η are presented in Fig. 2.8. A fit of experimental data to these theoretical curves can give the value of η (and consequently of ν_q from Eq. (2.9)).

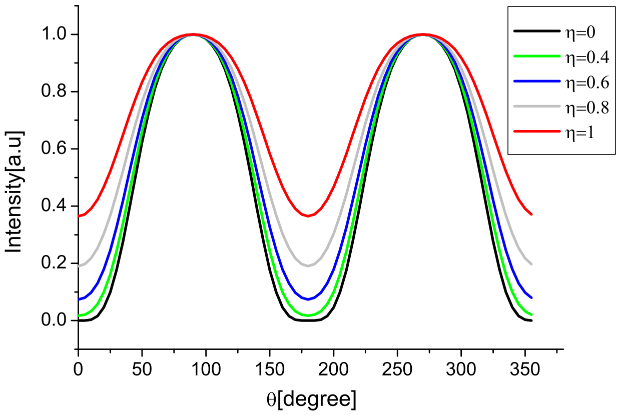

Figure 2.8: Theoretical echo intensity curves according to Eq.(2.29), for various values of η in an oriented powder, as a function of the polar angle θ between the RF field and the $\hat{z}$ direction of the EFG.

The advantages of this technique are: as in the nutation experiment, it allows the determination of η at every point of the NQR spectrum, and it allows the determination of η without the application of a magnetic field. This technique can be applied to all orientable powders. Its main weakness is that it is very insensitive to ηs smaller than 0.2.

2.5.1 The orientation of the EFG tensor

As mentioned before, For YBCO$_7$ it is known that the $\hat{c}$ axis of the lattice is perpendicular to the V_{zz} direction. For lower doping levels however, it in not necessarily the case. The calculations for the ADNQR method shown above are assuming that $V_{zz}\backslash\backslash\hat{c}$. There is a possibility however, that for lower doping V_{zz} is not exactly parallel to $\hat{c}$, and it has a component parallel to the ab plane (see Fig. 2.9).

For simplicity we choose the case of $\eta = 0$. In This case the NQR Hamiltonian is just:

$$H_Q(\eta = 0) = \frac{\hbar\nu_q}{6}[3I_z^2 - I^2]. \tag{2.30}$$

The rf pulse Hamiltonian is:

$$\mathcal{H}_{rf} = \gamma\hbar\mathbf{B}_1 \cdot I \sin\omega t, \tag{2.31}$$

where the rf field in an arbitrary direction is

$$\mathbf{B}(t) = 2B_1\left[\sin(\theta)\cos(\phi), \sin(\theta)\sin(\phi), \cos(\theta)\right] \tag{2.32}$$

θ and ϕ are the angels between the rf transmission and the EFG directions. In the experiment we rotate the $\hat{c}$ direction of the sample with respect to the rf transmission. If $\hat{c}$ and V_{zz} are not co-linear, then there can never be a case where $\theta = 0$. $\mathcal{H}_Q$ and $\mathcal{H}_{rf}$ do not commute, and therefore we will get a signal when transmitting along $\hat{z}$ even if η=0.

Hence, if the orientation of the EFG tensor differs from the one of YBCO$_7$ but η remains zero, we still expect the signal intensity ratio of the $\theta = 0$ and $\theta = \frac{\pi}{2}$ cases to be smaller than the theoretical prediction we gave in Fig. 2.8. In other words ADNQR is sensitive to either braking of the xy symmetry, or rotation of the principal axis from the $\hat{c}$ direction.

2.6 The experimental setup

The resonance experiments were done on YBCO$_y$ oriented powders, with different doping levels. The measurements were preformed at a temperature of 100K, which is above T_C for all samples. The data was collected using a spin echo sequence.

In the NMR experiment we measured the echo intercity as a function of H_0 with the rf frequency constant at 88MHz. In the echo sequence $t_{\pi/2}$ was 4μsec and τ was

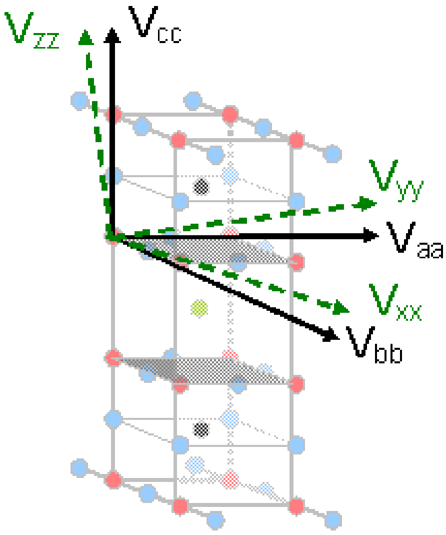
V_{zz}
V_{cc}
V_{yy}
V_{aa}
V_{xx}
V_{bb}

Figure 2.9: An illustration of a possible orientation on the EFG tensor with respect to the YBCO lattice.

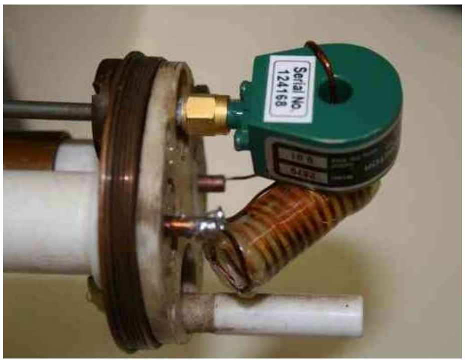

Figure 2.10: The nutation spectroscopy prob. The coil goes through a current monitor that allows measurements in different frequencies with the same current.

30μsec. The actual spectral points were obtained by signal averaging over 20480 scans.

In the NQR experiments, both for the nutation technique and for the ADNQR technique, there is great importance for the homogeneity of the rf field. For the nutation experiment we measured samples with small volume inside a long cylindric coil. For the ADNQR we used a spherical coil that gives a more homogenous field with a better filling factor.

The probe for the nutation spectroscopy experiment is shown if Fig. 2.10. The coil's wire goes through a current monitor. This current monitor, with a connection to an oscilloscope, allows us to perform all measurements with the same current in the coil, and therefore the same H_1. The sequence used in this experiment is shown in Fig. 2.11, with t_p changing from 0.3μsec to 150μsec. The refocusing pulse t_r was 4.4μsec and τ was 32μsec.

The ADNQR probe is shown in Fig. 2.12. As mentioned before, we used a spherical coil in order to get a more homogenous magnetic field. The coil is fixed to the

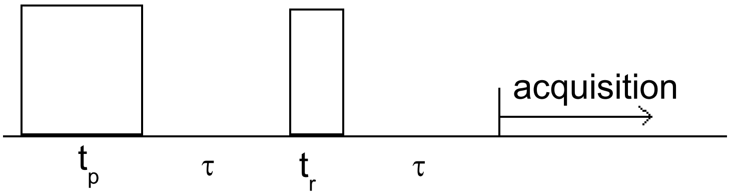

Figure 2.11: Pulse sequence for the nutation spectroscopy NQR.

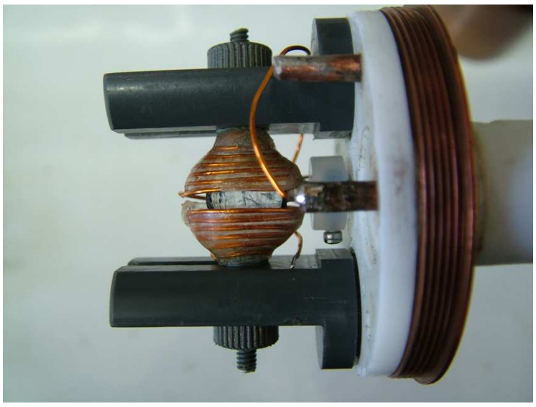

Figure 2.12: The ADNQR probe.

probe to minimize ringing. The experiment is fully automated, the sample holder is connected to a motor which rotates the sample and can be controlled from the computer. A computer program rotates the sample to the requested angle and then takes a measurement. The data was obtained by applying a spin echo sequence with $t_{\pi/2}$ of 2.3μsec and τ of 34μsec. The actual data points were obtained by signal averaging of 200,000 scans with a delay time of 3msec between scans. The measurements were performed in a coil tunable from 25 to 33MHz.

Chapter 3

Site assignment

Previous works with NQR on YBCO analyze the different resonance frequencies and associate them to different environments [29]-[32]. However, these experiments were preformed on YBCO with both isotopes (^{63}Cu and ^{65}Cu), and hence changes in the complicated spectrum (which will be reviewed next) due to doping, are harder to detect.

We measured [3] the NQR frequency sweep lines of YBCO$_y$ samples with different doping at 100K. The samples were all oriented, to enhance the signal intensity, and enriched with the Cu^{63} isotope as explained in section 2.1.1. The lines were obtained using a spectrometer with a home-made automated frequency sweep. The frequency sweep lines are presented in Fig. 3.1. The spectrum is normalized by f^2 in order to correct for population difference and the induced signal in the coil.

For each sample, the resonance frequencies were extracted from the frequency line, and plotted as a function of the superconducting transition temperatures T_c. This plot is presented in Fig. 3.3. From this plot it is clear that for our samples there are three different resonance peaks, each peak is shifted with doping. The different peaks

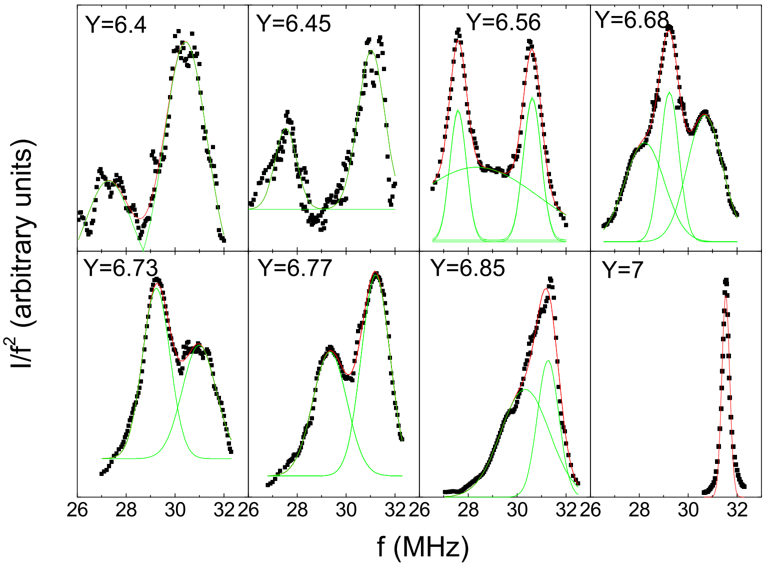

Figure 3.1: NQR frequency sweep on YBCO [3]. The dotted line is the experimental result. The solid line is a Gaussian fit performed in order to determine the resonance frequencies.

have different ν_q and therefore indicate to a different Cu cite.

We assigned the different resonance frequencies of each sample, based on the previous NQR and NMR measurements on YBCO [29]-[31]. We concluded that for high doping level ($y > 6.5$) all signals are from Cu(2) in the plane. There are three different types of environment that affect the Cu(2) resonance frequency. These three types of frequencies can be seen most clearly in the sample with $y = 6.68$. These frequencies were classified in terms of the number of oxygen surrounding the chain copper Cu(1) neighboring the detected Cu(2). When the chain is full ($Cu(1)_4$), as in $YBCO_7$, the frequency is highest. The lower frequency belongs to the Cu(2) whose neighboring Cu(1) is missing one oxygen ($Cu(1)_3$), and the lowest frequency is when the neighboring chain is empty ($Cu(1)_2$). The three possible environments of the

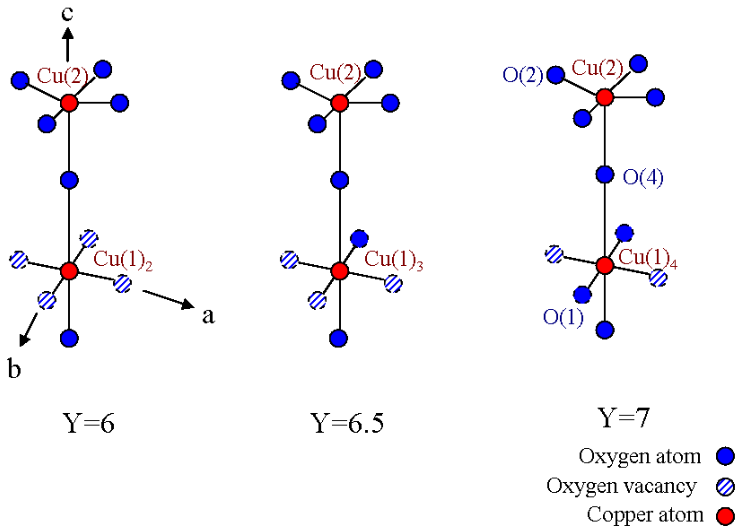
c
Cu(2)
Cu(1)₂
a
b
Y=6
Cu(2)
Cu(1)₃
Y=6.5
O(2)
Cu(2)
O(4)
Cu(1)₄
O(1)
Y=7
Oxygen atom
Oxygen vacancy
Copper atom

Figure 3.2: Schematic illustration of the Cu site with locally different oxygen coordinations.

Cu(1) are shown schematically in Fig. 3.2.

Fig. 3.3 show that for each Cu(2) environment, the shift in the resonance frequency is linear with T_c. If η does not change for each Cu(2) environment as a function of doping, then our results show a linear relation between T_c and ν_q. ν_q is proportional to the free charges around the nucleus. In that case can conclude that for YBCO the changes in T_C are proportional to the changes in the superfluid density. However from this standard NQR experiment, we could not determine ν_q and η.

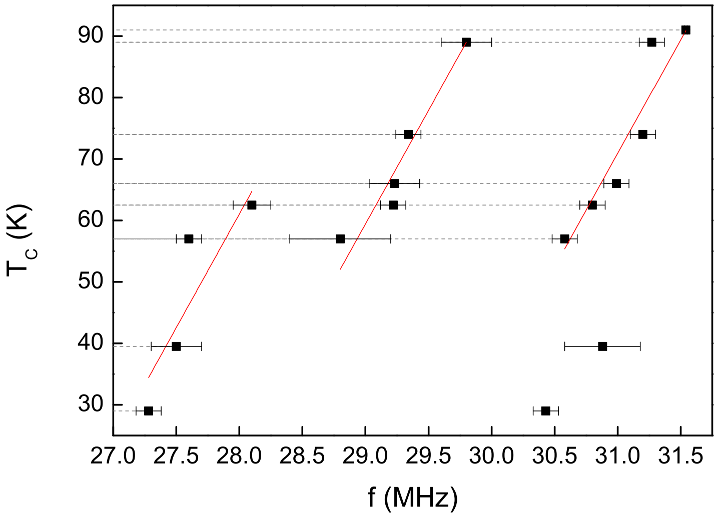

Figure 3.3: T_c for different YBCO samples as a function of the NQR frequencies. The solid lines are fits of the data to three lines with shared slope ($dT_c/df = 37 \pm 4$[K/MHz]).

Chapter 4

Results

4.1 NMR results

The Cu NMR spectra of 4 samples of YBCO$_y$ with different doping levels is shown in Fig. 4.1. All samples shown here are enriched with ^{63}Cu, and are in the form of oriented powder. The measurements were done with the external magnetic field perpendicular to the c axis.

This spectrum shows the central transition ($-1/2 \leftrightarrow 1/2$) with two peaks for the Cu(2) and Cu(1). According to previous NMR work [31][36] we can determine that the higher frequency belongs to the Cu(2) and the lower to Cu(1).

The spectrum also shows the low field quadrupolar satellite ($-3/2 \leftrightarrow 1/2$ transition). For $y = 7$ this satellite is relatively sharp and belongs to Cu(2). It is consistent with the line shape of $\eta = 0$. As the doping is lowered the spectrum becomes more complicated. At lower doping there is more then one Cu(2), as well as Cu(1) environments. Fig. 4.1 shows that as the doping decreases the satellite becomes a lot wider and weaker. For $y = 6.68$ the satellite is almost impossible to detect. Therefore NMR

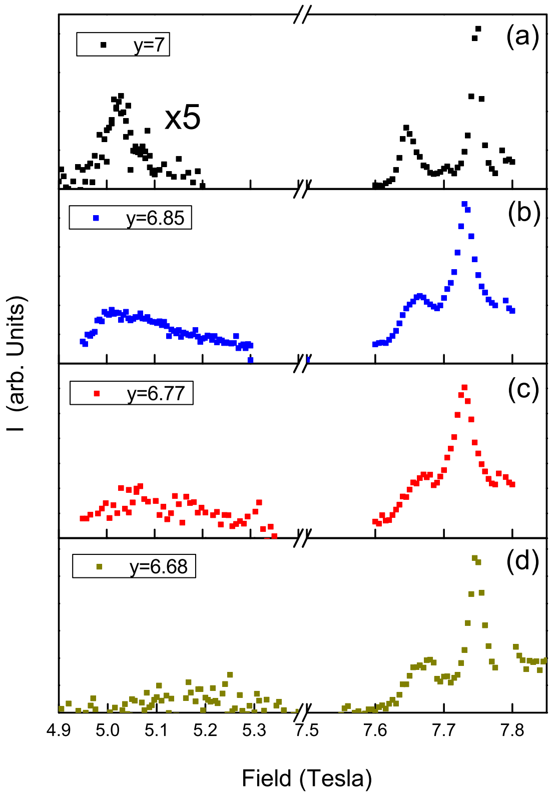

Figure 4.1: ^{63}Cu NMR spectra at 100K and 88MHz of different YBCO$_y$ samples. The satellites intensity is multiplied by a factor of 5.

can not be used in order to extract the asymmetry parameter for YBCO with $y \neq 7$. However the disappearance of the satellites as the doping is lowered can indicate that either η is larger at lower doping or there is a distribution of the EFG between the different environments.

4.2 Nutation Spectroscopy results

The nutation spectroscopy technique was applied for three YBCO$_y$ samples, the results are shown on the right panels of Fig. 4.2. For each sample the measurement was done in the frequencies marked with arrows on the NQR line shapes shown in the left panels. The nutation spectra is a result of measuring the echo intensity as a function of the first pulse length t_p and then Fourier transform.

For the Cu(2) of YBCO$_7$ it is known that the principal component of the EFG is in the c direction of the lattice and that $\eta = 0$. From Eq. (2.20) to (2.23) we know that for the case of $\eta = 0$ there is only one nutation frequency and the ratio ω_p/ω_1 is equal to 0.866. Hence, from the nutation frequency of the Cu(2) resonance line of YBCO$_7$ we can extract ω_1. Since we worked with a constant rf field H_1, we normalized the frequency axis for all samples by ω_1.

Fig. 4.2(d) shows the nutation spectrum for YBCO$_7$, measured in both the Cu(2) (31.5MHz) and the Cu(1) (22MHz) resonance frequencies. After normalizing the frequency axis by ω_1, we get for the Cu(2) one nutation frequency with $\omega_p/\omega_1 = 0.866$, and for the Cu(1) a much broader spectrum with $\omega_{pIII}/\omega_1 = 0.52$ and ω_{pII} is difficult to determine. These results are consistent with $\eta = 0$ for Cu(2) and $\eta = 0.95 \pm 0.05$ for Cu(1) (see theoretical nutation spectra in Fig. 2.6). This result is in agrement with NMR results on YBCO$_7$ [31][36] that measured $\eta \simeq 0$ for Cu(2) and $\eta \simeq 1$ for Cu(1). Similar nutation experiments on YBCO$_7$ at room temperature were done by Vega [2]. His results were $\eta = 0$ for the Cu(2) and $\eta = 0.8$ for the Cu(1).

Fig. 4.2(e) and (f) show the nutation spectroscopy results for YBCO$_y$ with lower doping levels. For these samples we measured only at the resonance frequencies of the Cu(2). The sample with $y = 6.73$ has two resonance lines for two Cu(2) ionic environments, and the sample with $y = 6.68$ has three Cu(2) environments (see chapter 3). The nutation experiment shows that for these samples, for all three different types of Cu(2) ionic environments, $\eta \simeq 0$. In the case of $\eta = 0$ the singularities ω_{II} and ω_{III} (Eq.(2.22),(2.23)) unit, there is only one singularity and the line shape is independent of the EFG orientation with respect to the rt pulse.

4.3 ADNQR results

The ADNQR technique was applied to two samples of YBCO$_y$ with $y = 7$ and $y = 6.68$. These samples' frequency lines are presented in Fig. 4.3(a),(b). The arrows in this figure mark the frequencies where ADNQR was applied.

The $y = 7$ sample used here was not enriched; hence there are two main resonance peaks at $f = 31.55$MHz for the Cu^{63} isotope and $f = 29.3$MHz for the Cu^{65} isotope. At this doping, the peaks from the different isotopes are well separated. The ADNQR was applied on the Cu^{63} peak and its two shoulders.

For the enriched $y = 6.68$ sample, the technique was applied to all three peaks. Each peak probes a different ionic environment, as explained in the previous chapter. We chose this sample because it contains all three environments. In addition, samples with a low doping level may contain a signal from Cu(1). This signal in YBCO$_6$ is at a frequency of ~ 30MHz. It is clear from Fig. 4.3(b) that there is no peak at this frequency for the $y = 6.68$ sample, and therefore the Cu(2) peaks of this sample are not contaminated by the Cu(1) signal.

The ADNQR results in Fig. 4.3(c),(d) show that the intensity at $\theta = 0$ and 180 is lower than at $\theta = 90$, as predicted in section 2.5. The solid lines in this figure are a fit of the experimental data to Eq. (2.29). The fit allows a finite base line for each

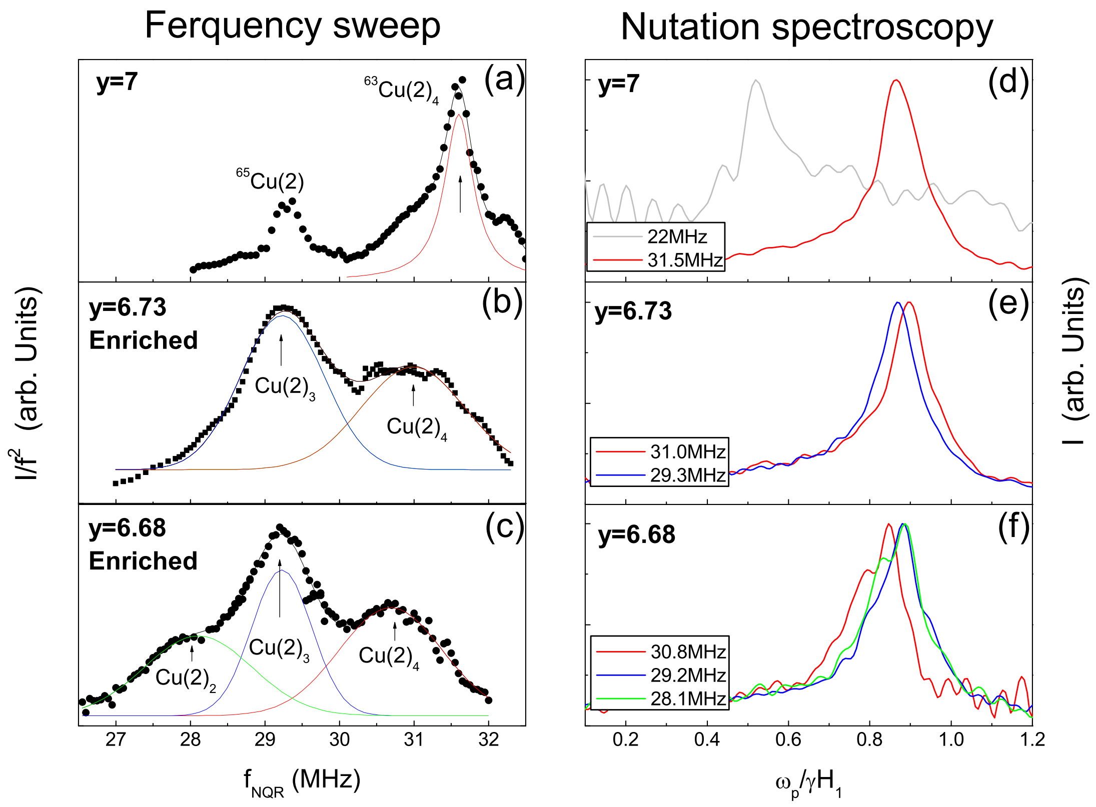

Figure 4.2: (a) Cu NQR line shape for $YBCO_7$ with natural abundance of ^{65}Cu and ^{63}Cu. (b) and (c) Cu NQR line shape for $YBCO_{6.73}$ and $YBCO_{6.68}$ enriched with ^{63}Cu. The arrows show the frequencies where nutation spectroscopy is applied. (d)(e) and (f) nutation spectra for these three samples.

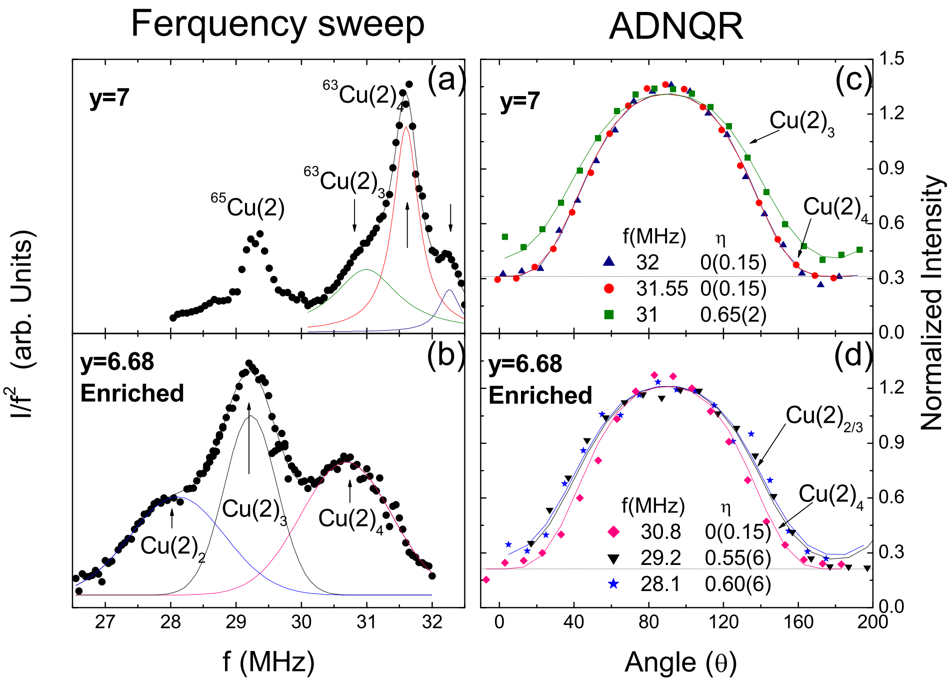

Figure 4.3: (a) Cu NQR line shape for YBCO$_7$ with natural abundance of ^{65}Cu and ^{63}Cu. (b) Cu NQR line shape for YBCO$_{6.68}$ enriched with ^{63}Cu. The arrows show the frequencies where ADNQR is applied. (c) and (d) The echo intensity as a function of the angle θ between the rf field and the principal axis of the EFG, for the two samples. The solid lines are fits to Eq. (2.29).

sample to account for some unknown amount of misalignment. This misalignment is a result of the non-perfect orientation and some inhomogeneity of the induced field in the coil.

The best fit for the main peak of $y = 7$ was achieved for $\eta = 0 \pm 0.15$, indicating that the CuO plane is charge homogeneous. Again, this result is in good agrement with previous results obtained from NMR giving values of: $\eta = 0$ [31] and $\eta = 0.01 \pm 0.01$ [36]. This result is also in agreement with our nutation spectroscopy results from the previous section.

The most interesting result is that obtained for $y = 6.68$. The best fit for the peak associated with an environment of a full chain also gives $\eta = 0 \pm 0.15$, despite the frequency shift. In contrast, for the other oxygen environments the signal as $\theta \rightarrow 0$ is clearly above the background, suggesting that the value of η is larger than zero. The fit to Eq. (2.29) gives $\eta \simeq 0.6$. One has to bare in mined however, that this fit assumes that the main EFG V_{zz} is in the $\hat{c}$ direction. As we discuss in section 2.5.1, an alternative explanation to the higher signal at $\theta = 0$ is that for these environments V_{zz} is not exactly parallel to the $\hat{c}$ direction. In that case even if $\eta = 0$ there is still a signal expected at $\theta = 0$ from the component of V_{zz} that is parallel to the plane.

Chapter 5

Discussion and Conclusions

In this part we compare three different techniques to measure the quadrupole interaction asymmetry parameter η. The techniques are employed on the in-plane Cu atom of the YBCO compound with different doping levels.

The first technique is the conventional NMR experiment. Cu NMR was preformed successfully in the past for YBCO$_7$, and the parameters ν_q, η and the knight shifts were extracted for both Cu(1) and Cu(2). For lower doping levels however, the spectrum becomes very complicated, due to different ionic environments that result from extracting oxygen from the chains.

In this work we attempted to simplify the spectrum by using enriched samples, containing only the ^{63}Cu isotope. We have seen however that as the doping level is lowered the satellites becomes very broad and weak, and this technique can not be used to extract the quadrupole interaction parameters for YBCO at lower doping. The broadening and disappearance of the satellites suggest however, that there is a distribution in the EFG parameters for the Cu(2).

Next we used two methods that use pure NQR experiment with no permanent magnetic field. The main advantage of these techniques is that they can be employed at every point of the NQR spectrum. Therefore, unlike NMR, η can be determined for each different ionic environment separately.

The nutation spectroscopy experiment showed that for YBCO$_7$ $\eta = 0$ for Cu(2) and $\eta \simeq 1$ for Cu(1), in agreement with previous NMR results. This experiment also showed that for lower doping levels, η remains zero, not only for the Cu(2) neighboring a full chain as in YBCO$_7$, but also for Cu(2) neighboring an empty or a half filled chain. This technique however is not sensitive to the EFG orientation.

Finally the ADNQR technique showed that for low doping levels there is a clear difference between the Cu(2) neighboring a full chain as in YBCO$_7$, and the Cu(2) neighboring an empty or a half filled chain. For the Cu(2) with full chain both for $y = 7$ and $y = 6.68$, the result was $\eta = 0$. However for the two other cu(2) environments of $y = 6.68$ the fit to the theoretical calculation gave $\eta \simeq 0.6$. This seems to be in contradiction to our nutation spectroscopy results. The way to setal the contradiction is to remember that the theoretical calculation of the ADNQR is based on the assumption that V_{zz} parallel to the c direction of the lattice. This assumption was confirmed for y=7 and y=6. It is possible that at other doping levels, for Cu(2) neighboring an empty or a half filled chain, V_{zz} is not exactly in the c direction (see Fig. 2.9), and as a result we get an enhancement of the signal at $\theta = 0$, although $\eta = 0$ (see section 2.5.1).

Our motivation for these experiments was to measure possible charge inhomogeneity or electronic phase separation in the YBCO compound. Both the nutation spectroscopy and the ADNQR for the Cu(2) from a fully oxygenized environment, even for lower doping, show a homogeneous charge distribution in the plane.

Our combined nutation and ADNQR experiment imply that the principle axis

z of the EFG tensor is not along c, therefore the symmetry in the CuO_2 planes of $YBCO_{6.68}$ neighboring a chain with missing oxygen, is lower than the one of $YBCO_7$. This means that any phase separation in the plane is correlated directly with the O dopant atoms, and therefore cannot be an intrinsic property of CuO planes.

McElroy *et.al.* [42] came to a similar conclusion by preforming spectroscopic imaging scanning tunneling microscopy on Bi-2212 samples. They found strong correlation between the position of localized resonance at -960meV identified with interstitial oxygen dopants and the size of local spectral gap.

To understand these result Nunner *et.al.* [43] presented a theoretical model where the dopants modulate the pair interaction locally on an atomic scale. They calculated the correlation between the local density of states and the dopant modulated pair interaction potential. They showed that this model agrees with McElroy's experimental results on Bi-2212. A more resent theoretical work by Mori *et.al.* [44] identified two mechanisms by which the position of the apical oxygens can modulate the pairing interaction within the CuO_2 planes.

Our result for the YBCO compound reinforces the surface experiments done on Bi-2212. It shows that the correlation between the electronic spatial variation in the plane and the dopant, exists not only in Bi-2212 and it is a property of the bulk and not only of the surface.

Chapter 6

Universal doping dependence of the ground state staggered magnetization in cuprates

In the second part of this thesis further underdope a cuprate until it becomes magnetic. We concentrate on differen families (x) of the HTSC compound $(\mathrm{Ca}_x\mathrm{La}_{1-x})(\mathrm{Ba}_{1.75-x}\mathrm{La}_{0.25+x})$C (CLBLCO). We determine the lattice parameters variations for all x and doping, and get an estimate for the t-J model energy scales from structural considerations. In addition, we measure the doping dependence of the ground state staggered magnetization for each CLBLCO family. These measurements provide alternative information on the t/J ratio.

All cuprate compounds have a layered structure with one or more copper-oxygen planes. The most simplified way to describe these planes is by the one band Hubbared

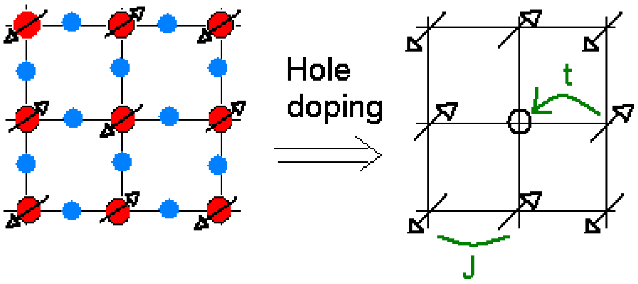

Figure 6.1: An illustration of The Cu-O plane in cuprates. On the left: The parent compound. The blue are the copper atoms and the red are the oxygen atoms. On the right: A simplified one band model of the electronic structure, with electrons hopping with hopping rate t. There is an AFM exchange J between spins on neighboring sites.

model with holes hopping on a square lattice [45][46].

$$\mathcal{H} = -\sum_{<i,j>\sigma} t_{i\sigma} c^{\dagger}_{i\sigma} c_{j\sigma} + U \sum_{i} n_{i\uparrow} n_{i\downarrow} \tag{6.1}$$

$c^{\dagger}_{i\sigma}$ is the creation operator of an electron with spin σ, t_{ij} is the hopping matrix element between sites i and j, and U is the repulsive energy cost due to screened Coulomb interaction to put two electrons with opposite spins on the same site. For the cuprates parent compounds there is one electron per site (half filling), and have a large $U >> t$. In this case the electrons prefer to be localized on the lattice site because hopping to reduce kinetic energy t will cost in U. This phase, called a Mott insulator, is described schematically in Fig. 6.1. This insulator is antiferromagnetic (AFM), since AFM alignment permits virtual hopping to gain an energy $J = 4t^2/U$, will for ferromagnetic alignment hopping is forbidden by the Pauli exclusion. In the doping process, holes are introduced into the copper-oxygen plans and the AFM order is rapidly destroyed by a few percent of holes.

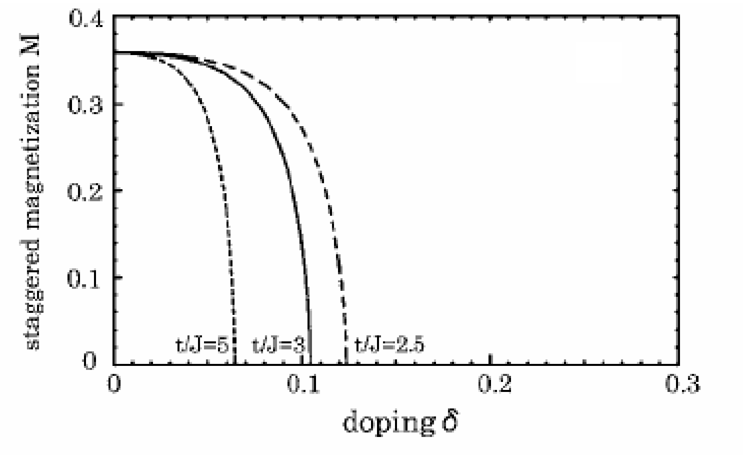

Figure 6.2: A Theoretical calculation of the doping dependence of the ground state staggard magnetization for different t/J, as calculated by Yamamoto *et al.* in Ref. [4].

It is widely agreed that cuprates should be addressed as a doped Mott insulator, where holes are moving on a 2D AFM background [47][48]. Since in this case $t << U$, it can be expand in t/U. The leading order is described by the t-J model Hamiltonian:

$$\mathcal{H} = -\sum_{i,j} t_{ij} c^{\dagger}_{i\sigma} c_{j\sigma} + H.c. + \sum_{i,j} J S_i \cdot S_j \tag{6.2}$$

where t and t' are the near and next-near neighbor hoppings, respectively, and J is the Heisenberg superexchange between local spins $S_i = c^{\dagger}_{i\alpha}\sigma_{\alpha\beta}c_{i\beta}$.

In this model, shown schematically in Fig. 6.1, if we look at a single hole hopping in an AFM background, one hop will cause the spin to be surrounded by ferromagnetic bonds. There is a competition between the energy cost in J and the gain of kinetic energy t. In the limit of low doping this competition causes the effective hopping rate to be renormalized from t to J [49][50][51][52].

Above some critical doping the zero temperature staggered AFM order parameter

M_0 is destroyed, and the cuprates enter a glassy, phase separated, state. Since the glassy state precedes superconductivity, understanding this transition is crucial to understanding the cuprates. Particularly interesting is the doping dependence of M_0 and its variations with the different energy scales. These variations were calculated theoretically [53][54][55][4] but not measured in a controlled manner. An example for one of these calculations, done by Yamamoto *et al.*, is shown in Fig. 6.2. Such measurements could shed light on the effective Hamiltonian governing the holes at $T \to 0$ in the underdoped region. While J can be measured relatively simply with neutron or Raman scattering on a single crystal, it is very difficult to determine t experimentally.

In this work we determine t/J from lattice parameters, including the buckling angle, using neutron powder diffraction. We determine the doping dependence of M_0 using zero field muon spin rotation (μSR).

Chapter 7

The experimental methods

7.1 The CLBLCO System

$(\mathrm{Ca}_x\mathrm{La}_{1-x})(\mathrm{Ba}_{1.75-x}\mathrm{La}_{0.25+x})\mathrm{Cu}_3\mathrm{O}_y$ is a HTSC, which also belongs to the 1:2:3 systems. In comparison to YBCO, Ca occupies the Y site, and La occupies both the Y and the Ba sites (see Fig. 7.1).

The family index x varies in the range $0.1 \leq x \leq 0.4$. All compounds are tetragonal and there is no chain ordering as in YBCO [56]. The oxygen atoms in the Cu(1) layer are distributed randomly with respect to the a and b directions. The CLBLCO compound is stable throughout all parabolic T_C curves, so one can synthesize samples ranging from the underdoped to the overdoped, by changing the O doping. As we show below, there are minimal structural differences between the families. In addition, the level of disorder as detected by Ca NMR [57] and Cu NQR [58] is identical for the different families.

The phase diagram is presented in Fig. 7.2 showing the antiferromagnetic Néel temperature T_N, the spin glass temperature T_g where islands of spins freeze, and the

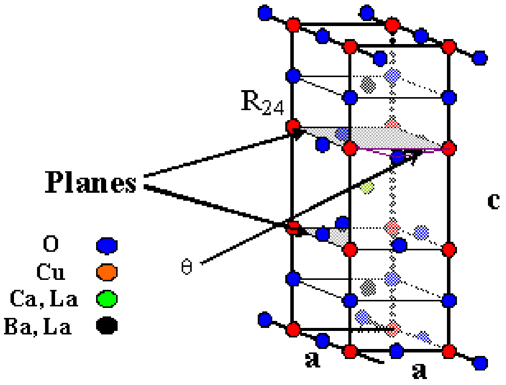

Figure 7.1: The $(Ca_xLa_{1-x})(Ba_{1.75-x}La_{0.25+x})Cu_3O_y$ (CLBLCO) unit cell.

superconducting critical temperature T_c. In this phase diagram T_N [59] and T_g [60] were measured by μSR, and T_c was measured by resistivity [56]. The spin glass phase penetrates into the superconducting phase. It also slightly penetrates into the Néel phase in the sense that a first transition, to long range order, takes place near 200 K, and a second transition, with additional spontaneous fields, takes place near 10 K.

7.1.1 Sample preparation

The CLBLCO samples are also prepared by solid state reaction, as described in chapter 2.1.1 for YBCO. The oxygen reduction at high doping levels is done in the same way as in the YBCO samples, in a tube furnace in flowing oxygen. Under a certain doping level (about y=6.7), the reduction is made with flowing nitrogen instead of oxygen (so that more oxygen can come out of the sample at a certain furnace temperature), and quenched to room temperature.

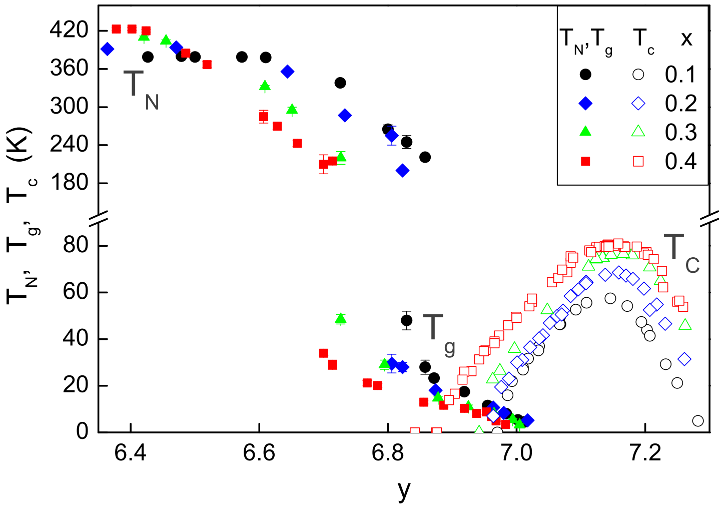

Figure 7.2: The CLBLCO phase diagram including magnetic (close symbols) and superconducting (open symbols) critical temperatures.

7.2 Neutron powder Diffraction

Neutron scattering is a very useful technique in the study of materials. The thermal neutron has a magnetic moment, no electrical charge, it's wavelength is comparable to that of interatomic distances, and it's energy is of the order of the thermal excitations of crystals. These properties make it suitable for the study of both structural and dynamical aspects of matter.

In scattering experiments, the conservation rules, momentum and energy, are:

$$\mathbf{Q} = \mathbf{k}_F - \mathbf{k}_I \qquad h\nu = E_F - E_I \tag{7.1}$$

I and F subscripts stand for the initial and final state of the neutron. The wave vector is $k = \frac{2\pi}{\lambda}$ and the energy is the classical kinetic energy, $E = \frac{1}{2}mv^2$. Assuming an elastic scattering, $(hv = 0)$ we have $|\mathbf{k}_F| = |\mathbf{k}_I| = \frac{2\pi}{\lambda}$ and the scattering vector $\mathbf{Q} = \frac{4\pi}{\lambda} sin\theta$, θ being half the scattering angle.

In a neutron powder diffraction experiment the Bragg reflections are used to get information on the crystal structure. The dynamical and magnetic aspects of the neutron-matter interaction are ignored. The experiment measures the scattered wave intensity as a function of the scattering angle (or Q).

7.2.1 Rietvelt refinement

The Rietvelt refinement [61] is a method to fit the powder diffraction experimental pattern and the calculated one. In this method the least-square refinement is carried out until the best fit is archived. The calculated pattern takes into account all of the parameters of the instrument and the sample, such as lattice parameters, atomic positions, and Debye-Waller factors (for thermal motion of the atoms).

In this method the calculated powder diffraction pattern is made out of a collection of individual reflection profiles, each with is own peak position, height, width, and area that is proportional to the Bragg intensity. Each atom's Bragg intensity I_k (k stands for the Miller indices (hkl)) is proportional to the square of the absolute value of the structure factor $|F_k|^2$.

The diffraction profile is calculated and compared with the observed pattern point by point. The parameters of the model are then adjusted using the least-squared method until a minimum is achieved. The quantity minimized in this method is:

$$S_y = \sum \frac{1}{I^i_{obs}} (I^i_{obs} - I^i_{calc})^2, \tag{7.2}$$

where I^i_{obs} is the observed intensity at the ith step, I^i_{calc} is the calculated intensity at the ith step, and the sum is over all data points.

In this work the refinement was done using the GSAS program [62] with the EXPGUI interface [63].

7.3 Muon Spin Rotation (μSR)

μSR is a technique that allows the study of magnetic properties of materials in a microscopic level. In this technique a beam of muons is injected into the matter. Each muon's spin then rotates around the local magnetic field, and then decays to a positron in the direction of the muon spin. The decayed positron direction in time indicates the muon's spin time evolution. The μSR experiments in this work were performed at the Paul Scherrer Institute (PSI) in Switzerland. The samples were measured in a ^{4}He cryostat. The samples were all sintered pellets. All the measurements were performed in zero field.

7.3.1 Muon production, implantation and decay

Experiments in condensed matter require high intensities and flux, this is achieved by using high energy proton beams, produced in cyclotrons. The protons collide with nuclei in an intermediate target and produce pions via:

$$p + p \rightarrow \pi^+ + p + n, \tag{7.3}$$

the pions then decay into muons:

$$\pi^+ \rightarrow \mu^+ + \nu_\mu, \tag{7.4}$$

where ν_μ is the muon-neutrino.

The muon beam is generated from pions decaying at rest in the target surface. These muons, known as surface muons, have zero momentum. Therefore, in order to conserve momentum, the muon and the neutrino have opposite spins. The neutrino always has negative helicity (its spin is antiparallel to its momentum), and thus the muon spin has to be similarly aligned. In this way a muon beam that is 100% spin polarized can be produced. The muons hit the target with energy of 4MeV, and lose their energy very quickly (in 0.1-1nsec) by various scattering processes, all of Coulombic origin, so there is no influence on the muon's spin. After stopped, the muons precess according to the local magnetic field and decay after a time t with probability $e^{t/\tau}$. $\tau = 2.2\mu$sec is the lifetime of the muon. The muon decays in a three body process:

$$\mu^+ \rightarrow e^+ + \nu_e + \bar{\nu}_\mu, \tag{7.5}$$

The decay is via the weak interaction and violates parity. This leads to the positron being emitted preferentially along the direction of the muon's spin at the time of the decay. The polarization of an ensemble of muons can be followed, by detecting the emitted positrons.

7.3.2 Experimental setup

Muon experiments can de performed in two different ways, depending on the time structure of the muon beam. In a Continuous Wave (CW) facility the muons arrive at the sample without any distinct time structure. When the muon enters the experiment it is detected and starts a clock. When the positron is detected in one of the detectors, the clock is stopped. The advantage of this type of muon beam is that the time resolution is quite good, and fast relaxing signals can be detected. On the other hand, if a second muon arrives before the first one has decayed then there is no way of knowing whether the emitted positron came from the first or second muon, so this event must be disregarded. This limits the maximal time for which the polarization of the muons can be traced to about 10μsec. In pulsed beam facilities, a large number of muons arrive in a very intense pulse and there is no need to detect when each muon arrives. The detection of the positrons is then made and each event is timed with respect to the arrival of the pulse. In this method the entire incoming muon intensity can be used and there is almost no background in the μSR signal. This allows detection of longer muon decay events. The drawback of this method is that the width of the muon pulse limits the time resolution. In this work we measured fast relaxing signals, hence the time resolution at the beginning of the signal was very important. Therefore we chose to preform our measurements in a CW facility at the Paul Scherrer Institute in Switzerland.

Once implanted in the sample, the muon spin precesses in the presence of the local magnetic field B with angular frequency $\omega_\mu = \gamma_\mu B$, where γ_μ is the gyromagnetic ratio for the muon. This is known as Larmor precession. Unlike other resonance techniques, like NMR or ESR, no electromagnetic field is necessary, since the muon beam is initially polarized, and the precessing muon can be followed directly from the emitted positron.

A schematic diagram of the experiment is shown in Fig 7.3. A muon, with its polarization aligned antiparallel to its momentum, is implanted in a sample. If it decays immediately, then it will not have time to precess and a positron will be emitted preferentially into the backward detector. If it lives a little longer it will have time to precess so that if it lives for half a revolution the resultant positron will be preferentially emitted into the forward detector.

Fig. 7.4 shows the time evolution of the number of positrons detected in the forward and backward detectors. Because the muon decay is a radioactive process these two terms sum to an exponential decay, with a decay constant that is the lifetime of the muon. The time evolution of the muon polarization can be extracted from the normalized difference between the number of positrons detected at the forward and

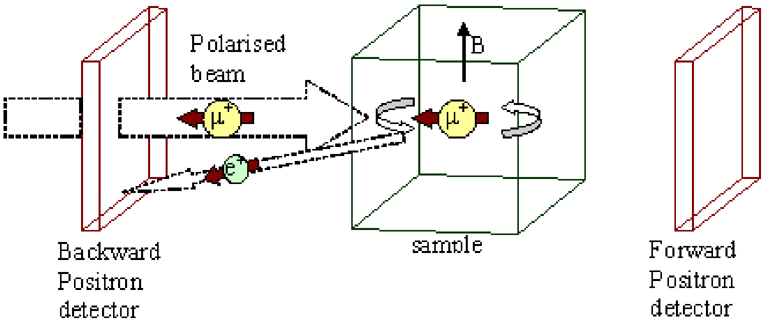

Figure 7.3: A schematic diagram of the MuSR experiment. A muon, with its polarization aligned antiparallel to its momentum, is implanted in the sample. It then rotates about the local magnetic field B with the Larmor frequency, and decays to a positron preferentially along the direction of the muon's spin at the time of the decay.

backward detectors,

$$A(t) = \frac{N_B(t) - \alpha N_F(t)}{N_B(t) + \alpha N_F(t)}. \tag{7.6}$$

α ia a parameter that corrects for geometrical differences between the detectors. $A(t)$ is called the asymmetry plot. The maximum value of the asymmetry plot depends on the initial beam polarization, the intrinsic asymmetry of the weak decay, and the exact structure of the detectors system.

μSR can be performed with no applied external field (ZF), as was done in this work, or with either transverse (TF) or longitudinal (LF) fields applied with respect to the initial muon spin direction. In the ZF case the muons will precess according to the internal field in the sample under study and reveal the internal field distribution. This method is very sensitive to detecting weak internal magnetism. In the TF case the muon will precess about the applied field, with frequency proportional to the size

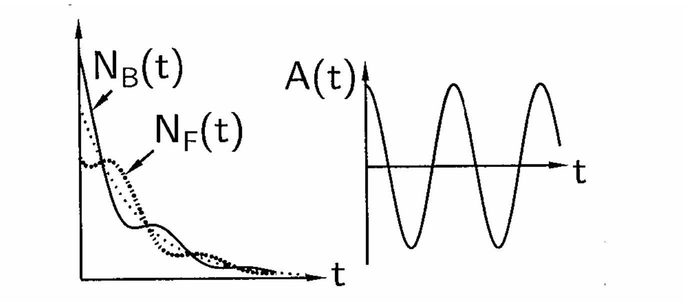

Figure 7.4: On the Left: The number of positrons detected in the forward and backward detectors. On the right: The muon Asymmetry function.

of the field at the muon site in the material. Any dephasing in the observed oscillation indicates either an inhomogeneous internal field distribution or spin-spin (T_2) relaxation. In LF there is no spin precession, but spin relaxation, due to inhomogeneous field distributions or spin-lattice (T_1) relaxation processes.

7.3.3 Muons in matter in Zero Field

Muons in magnetically ordered materials precess in the internal magnetic field and result in signals proportional to that magnetic field. The very large magnetic moment of the muon makes it very sensitive to extremely small magnetic fields (0.1G), and so it is useful in the study of materials where the magnetic order is random or very short range.

Fig.7.5 shows the muon-spin precession in a magnetic field. If the local magnetic field at a muon site is at an angle θ to the initial muon spin direction when the muon is implanted, the muon spin will precess around a cone of angle θ about the magnetic

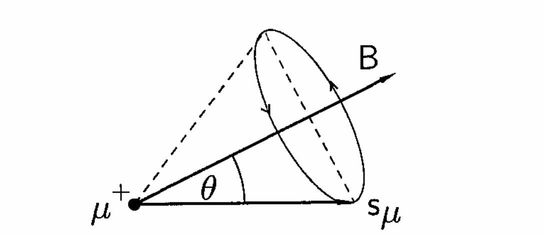

Figure 7.5: The muon spin precession about the magnetic field at an angle θ.

field. The polarization in the z direction (and the positron asymmetry) will be:

$$G(t) = \cos^2(\theta) + \sin^2(\theta)\cos(\gamma_\mu B t). \tag{7.7}$$

If the direction of the local magnetic field is random then averaging over all directions gives:

$$G(t) = \frac{1}{3} + \frac{2}{3}\cos(\gamma_\mu B t). \tag{7.8}$$

If the strength of the local magnetic field has a Gaussian distribution with width Δ/γ_μ centered on zero, then averaging over this field distribution gives:

$$G(t) = \frac{1}{3} + \frac{2}{3}e^{-\Delta^2 t^2/2}(1 - \Delta^2 t^2). \tag{7.9}$$

This polarization is known as the Kubo-Toyabe polarization, shown in Fig. 7.6. This relaxation function is observed experimentally in cases where the origin of the internal field is frozen random nuclear magnetic moments. A different form of the internal field distribution would change the form of the relaxation line.

Magnetic and non magnetic regions co-existing in the same specimen result in distinct signals whose amplitudes are proportional to the volume of the sample occupied by the particular phase.

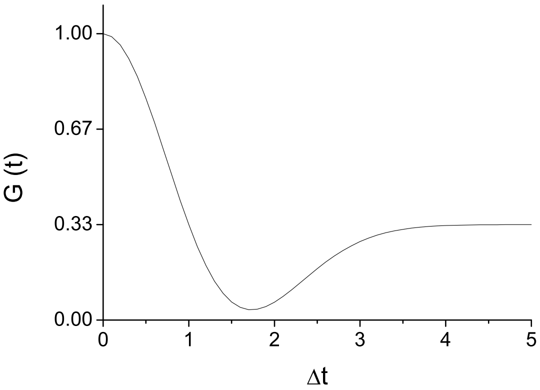

Figure 7.6: The Kubo-Toyabe polarization, the relaxation of the muon-spin due to a Gaussian field distribution.

Chapter 8

Summary of Our Previous μSR Results

In a previous work [59] we measured the magnetic transition temperatures T_N and T_g for the CLBLCO compound and constructed the phase diagram shown in Fig. 7.2. In that work, in order to interpret the phase diagram, we used a scaling relation.

The scaling was designed so that the T_c domes of all families, normalized by T_c^{max}, will collapse on to a single dome. For this purpose the mobile hole parameter measured from optimum Δp_m was defined by $\Delta p_m = K(x) \cdot (y - y_{max})$, where y_{max} is the optimal oxygen doping, and $K(x)$ is a family-dependent scaling parameter. K should be thought of as doping efficiency parameter connecting oxygen level to mobile holes in the CuO_2 planes. The best scaling was found using $K = 0.76, 0.67, 0.54, 0.47$ for $x = 0.1 \ldots 0.4$, respectively, and is shown in Fig. 8.1.

Despite the fact that $K(x)$ was chosen to scale the T_c domes, when applying it for the entire phase diagram the other critical temperatures scale as well. Fig. 8.1 also shows, T_g/T_c^{max} and T_N/T_c^{max}, for all families, as a function of Δp_m. The T_g/T_c^{max}

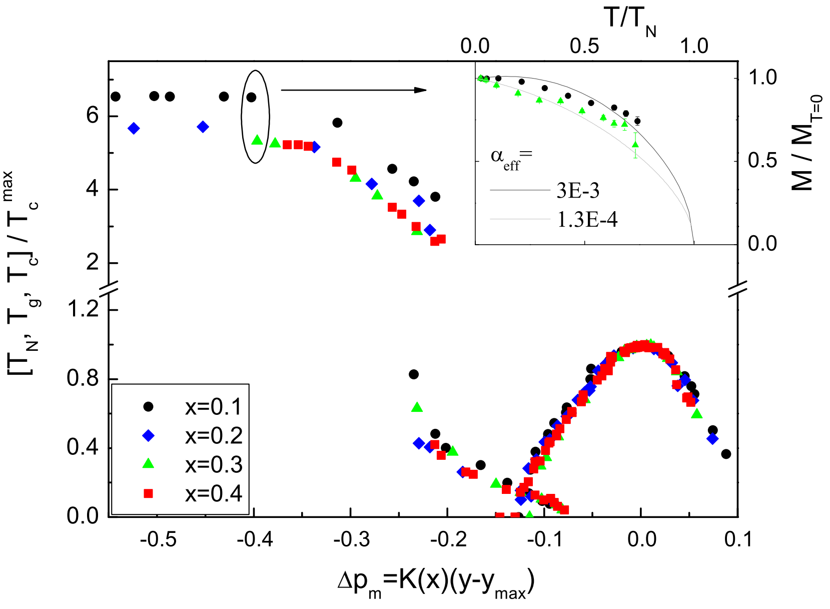

Figure 8.1: The CLBLCO phase diagram after scaling: For each family (x), the critical temperatures are normalized by T_c at optimal doping, and y is replaced by Δp_m (see text for details). Inset: The normalized staggered magnetization as a function of the normalized temperature. The symbols are the experimental results, taken by measuring the oscillation frequency of the polarization curves. The solid lines are the theoretical curves plotted according to Eqs. 8.2 to 8.5.

curves of all families collapse onto each other. The T_N/T_c^{max} curves, with the exception of the $x = 0.1$ family, also collapse onto each other. The reason T_N of the $x = 0.1$ family is not in-line with the others is due to interactions between planes, as explained next.

The Néel temperature stems from three dimensional interaction, and it is a function of not only the in-plane J, but also interplane couplings $J_\perp$ and other anisotropies. To account for the anisotropies quantitatively we assumed that CLBLCO could be considered a 2D magnet with weak anisotropies, since the chain layers are partially

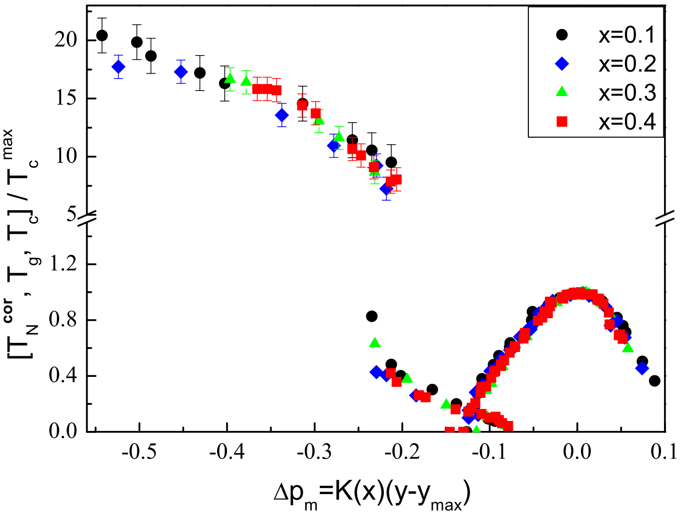

Figure 8.2: The same as Fig.8.1 but the Néel temperature is corrected for anisotropy contribution so it is the same as J for the parent compound (see text).

full with oxygen even for the parent compounds. Therefore we used the Hamiltonian

$$\mathcal{H} = J(\sum_{i,\delta_{\|}} \mathbf{S}_i \cdot \mathbf{S}_{i+\delta_{\|}} + \alpha_{xy} \sum_{i,\delta_{\|}} S_i^z S_{i+\delta_{\|}}^z + \alpha_{\perp} \sum_{i,\delta_{\perp}} \mathbf{S}_i \cdot \mathbf{S}_{i+\delta_{\perp}}) \tag{8.1}$$

where $\delta_{\|}$ and $\delta_{\perp}$ are the in and out of plane neighbor spacings, respectively.

In the Heisenberg model for the parent compounds, $T_N = Jt_N(\alpha_{eff})$ where the effective anisotropy α_{eff} is mainly set by $\alpha_{\perp}$, and $t_N(\alpha_{eff})$ is a known logarithmic function of the anisotropy [64][65]. We determined α_{eff} and extracted J from T_N. This was done by measuring the temperature dependence of the muon rotation frequency $\omega(T)$, which is proportional to the order parameter $M(T)$. The plot of M/M_0 as a function of T/T_N depends only on α_{eff}. The theoretical behavior of $M(T/T_N)/M_0$ was calculated using the self-consistent Schwinger-boson mean-field (SBMF) theory [64],[65]. The calculation was done by solving simultaneously for every α_{eff} and t

two equations: a self consistency equation

$$h = 2\alpha_{eff}\left[1 - 2K(\Delta, h, t)\right], \tag{8.2}$$

and a constraint equation ensuring one Schwinger-boson per site

$$K(\Delta, h, t) + K(\Delta, 0, t) = 1. \tag{8.3}$$

In these equations

$$K(\Delta, h, t) = 2.32\int_0^1 \frac{(1+\Delta+h)}{\omega(\Delta, h, \gamma)}\left[n(\omega(\Delta, h, \gamma), t) + 1/2\right]\rho(\gamma)d\gamma, \tag{8.4}$$

the density of states is given by

$$\rho(\gamma) = \frac{2}{\pi^2}\int\limits_0^1 \left[(1-t^2)(1-t^2+\gamma^2 t^2)\right]^{-1/2} dt, \tag{8.5}$$

or its approximation [66], $\omega(\Delta, h, \gamma) = 2.32((1+\Delta+h)^2 - \gamma^2)^{1/2}$, and $n(\omega, t) = \left[\exp(\omega/t) - 1\right]^{-1}$. Finally, $M/M_0(\alpha_{eff}, t) = h(\alpha_{eff}, t)/h(\alpha_{eff}, 0)$.

The inset of Fig. 8.1 shows $\omega(T/T_N)/\omega(T \to 0)$ for two samples marked in Fig. 8.1, and a fit to the predicted behavior described above. When comparing theory and experiment we focused on the low temperature data, up to 200 K, where the theory is most accurate. The $x = 0.1$ sample clearly has a bigger α_{eff} than the $x = 0.3$ sample, and is more 3D like. Using this method we determined α_{eff} for all samples with Néel order and defined the quantity

$$T_N^{cor} \equiv T_N/t_N(\alpha_{eff}) \tag{8.6}$$

for these samples [59]. For zero doping $T_N^{cor} = J$. When the system is doped, T_N is also affected by hopping and $T_N^{cor} = J$ is no longer valid. Fig. 8.2 shows the scaled phase diagram, where T_N is replaced by T_N^{cor}. After this replacement the entire phase diagram scales to a single unified curve, indicating that $T_c^{max} \propto J$ and that a single energy scale controls magnetism and superconductivity.

Chapter 9

Results

9.1 Neutron Diffraction results

The neutron powder diffraction experiments were performed by Omar Chmaissem at the Special Environment Powder Diffractometer at Argonne's Intense Pulsed Neutron Source.

The experiments were preformed on samples from 4 different families of CLBLCO. An example of a raw data and refinements for one of these samples is shown in Fig. 9.1. For each sample we used the refinement to extracted the lattice parameters, bond lengths and angels.

We looked for the parameters that are family-dependent and can potentially explain the different energy scales between the families. Fig. 9.2 shows a summary of the parameters extracted form the neutron diffraction experiment. The empty symbols represent data taken from Ref. [5]. These parameters are shown in the sketch of the CLBLCO unit cell in Fig. 7.1. All the parameters are family-dependent, however, not to the same extent. The lattice parameters a and c, depicted in Fig. 9.2(a) and (b),

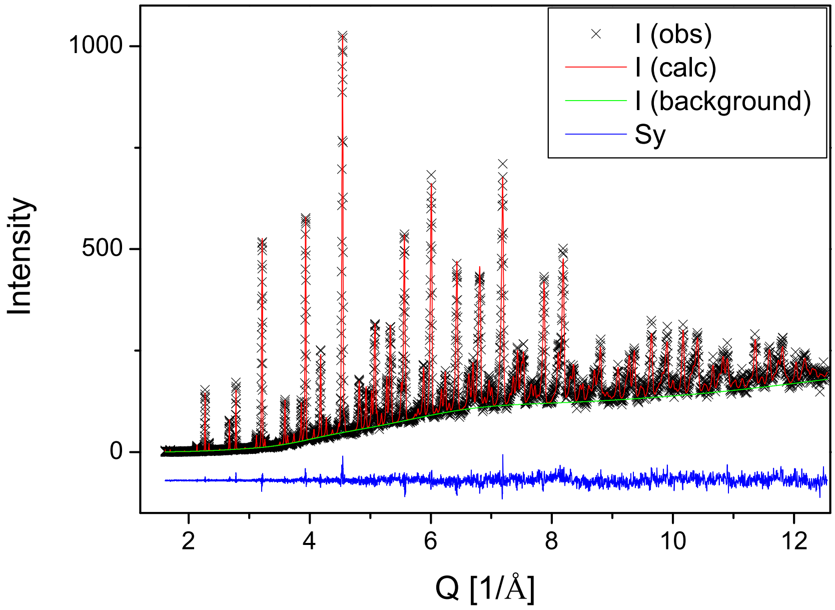

Figure 9.1: Neutron powder diffraction data and refinement for a sample with x=0.1 and y=7.06.

change by up to about 0.5% between the two extreme families ($x = 0.1$ and $x = 0.4$). The in-plane Cu-O-Cu buckling angle is shown in Fig. 9.2(c). This angle is non-zero since the oxygen is slightly out of the Cu plane and closer to the Y site of the YBCO structure. The buckling angle shows strong variation between the families; there is about a 30% change from the $x = 0.1$ family to $x = 0.4$. This change is expected since as x increases, a positive charge is moving from the Y to the Ba site of the YBCO structure, pulling the oxygen toward the plane and flattening the Cu-O-Cu bond.

We believe that this buckling angle is the main cause for the different J and therefore different T_c^{max} between the CLBLCO families [59]. Nevertheless, we note that Pavarini *et al.* [67] showed that in many cuprates families T_c^{max} scales with

t'/t. t' is controlled by the hybridization of the Cu 4s with the apical oxygen 2p$_z$, hence T_c^{max} scales with the distance R_{24} between the in-plane copper and the apical oxygen. In Fig. 9.2(d) we show R_{24} for our CLBLCO samples. Our results also support qualitatively Pavarini's conclusion.

From the lattice parameters and the buckling angle it is possible to construct t and J [68]. The hopping rate t_{dd} between two Cu $3d_{x^2-y^2}$ can be described as a hopping from the first Cu $3d_{x^2-y^2}$ to the O $2p$, followed by a hopping from the O $2p$ to the second Cu $3d_{x^2-y^2}$. It can be calculated from:

$$t_{dd} = \frac{\langle d_b|V|p\rangle\langle p|V|d_a\rangle}{E_d - E_p} \tag{9.1}$$

$$\langle p|V|d_a\rangle = t_{pd} \tag{9.2}$$

$$\langle d_b|V|p\rangle = t_{pd}\cos\theta \tag{9.3}$$

θ is the buckling angle between the bonds.

The charge transfer energy Δ is

$$\Delta = E_d - E_p \tag{9.4}$$

therefore,

$$t_{dd} = -\frac{t_{pd}^2\cos\theta}{\Delta} \tag{9.5}$$

The hopping integral t_{pd} between a Cu $3d_{x^2-y^2}$ and O $2p$ is proportional to bond length to the power -3.5 [69]. Therefore, assuming the charge transfer energy Δ is family-independent, we can estimate the hopping rate t_{dd} from:

$$t_{dd} \propto \frac{\cos\theta}{a^7}. \tag{9.6}$$

The superexchange J is known to be [**?**]:

$$J = \frac{4t^2}{U}. \tag{9.7}$$

Therefore, assuming that the Hubbard U is also family-independent:

$$J \propto \frac{\cos^2\theta}{a^{14}}. \tag{9.8}$$

Estimates of t_{dd} and J, normalized to the averaged values of the $x = 0.1$ family $\langle t_{dd}\rangle_{0.1}$ and $\langle J\rangle_{0.1}$, are presented in Fig. 9.3(a) and (b). Although there is a variation in t and J within each family, the variation is much larger between the families. J increases with increasing x, in qualitative agreement with our result for T_N^{cor} discussed in chapter 8.

In Fig. 9.3(c) we show the normalized ratio t/J for the four CLBLCO families. There is about 5% difference between the two extreme families. But we stress that this determination of t/J is only an estimate, used in practice to set the oxygen level spacing between samples in the μSR experiment discussed in the next section. More accurate calculations of t/J are in progress and preliminary data indicate that t/J varies by more than 10% between families [70].

9.2 μSR results

In this section we determine the doping dependence of the order parameter in the four CLBLCO families using zero field μSR. The experiments were done on the GPS beam line at the Paul Scherrer Institute, Switzerland. The muon oscillation frequency ω is proportional to the local magnetic field it experiences. Therefore, it can be used to determine the staggered magnetization M.

In general the polarization curves in this material can be described by a sum of two functions [59]. The first function is the Kubo-Toyabe function shown in Fig. 7.6 This part describes the polarization resulting from frozen random nuclear magnetic moments. The second function is a rapidly relaxing function that is a result of the magnetic field due to frozen electronic moments in the magnetic areas.

In this work are interested in the order parameter at $T \to 0$ therefore we performed the measurements at low temperatures, well bellow the magnetic transition. In these temperatures the Kubo-Toyabe function is undetectable and one can only see the fast relaxation du to the freeze of the electronic moments. The behavior at very low T indicates the nature of the ground state. For the antiferromagnetic ground state the long range order is reflected by spontaneous oscillations of the muon polarization in a addition to the fast relaxation. The spin glass ground state consists of magnetic islands with randomly frozen electronic moments [60], and consequently, the polarization shows only rapid relaxation.

Typical muon polarization curves at $T = 5$ K are presented in Fig. 9.4 for four samples from the $x = 0.4$ family. The sample in inset 9.4(a) is in the spin glass phase; it has no long-range magnetic order and hence has no oscillations. The sample in inset 9.4(d) is in the antiferromagnetic phase, and so it has strong oscillations at low temperatures. Finally, the samples in inset 9.4(b) and (c) are examples of intermediate samples and thus have weaker oscillations.

The best fit of the polarization is achieved with the function

$$P(t) = \sum_{i=1}^{3} A_i \exp(-\lambda_i t) \cos(\omega_i t) \tag{9.9}$$

with $\omega_3 = 0$; the fit is shown in Fig. 9.4 by the solid line. The reason for multiple frequencies is that the muons stop at different sites in the unit cell. The order parameter extracted from the high frequency, around a few tens of MHz, is known to agree with neutron scattering experiments [71]. The lower frequency is believed to emerge from metastable muon sites and is not used for further analysis.

The muon polarization was measured at low temperatures, typically from 5 K to 200 K, and the oscillation for $T \rightarrow 0$ was extracted from extrapolation. Fig. 9.5(a) shows a summary of the oscillation frequency $\omega(T \rightarrow 0)$ as a function of the chemical doping y for all four CLBLCO families. In this plot the AFM critical doping, where the oscillations disappear, is different for each family. Not surprisingly, this is the same oxygen doping where the Néel order is replaced by the spin glass phase in the diagram. However, the chemical doping is different from the mobile hole doping p_m, and a rescaling of the doping axis is required.

Fig. 9.6(a) shows $\omega(T \rightarrow 0)$ as a function of Δp_m for each family. The scalability of the phase diagram, as explained in chapter 8, suggests that Δp_m is a parameter proportional to the mobile hole density variation. Hence Fig. 9.6(a) is equivalent to a plot of the AFM order parameter at zero temperature as a function of mobile hole density.

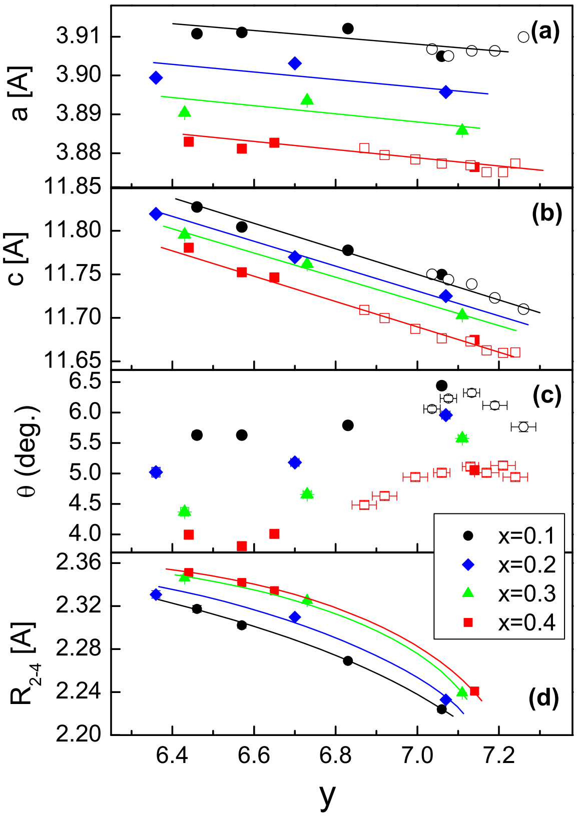

Figure 9.2: The parameters extracted from a neutron diffraction experiment as a function of oxygen doping for the four families of CLBLCO. (a) The lattice parameter a. (b) The lattice parameter c. (c) θ - the buckling angle between the copper and oxygen in the plane. (d) R_{24} - The distance between the in-plane copper and the apical oxygen. The empty symbols are measurements taken from [5]. The lines are guides to the eye.

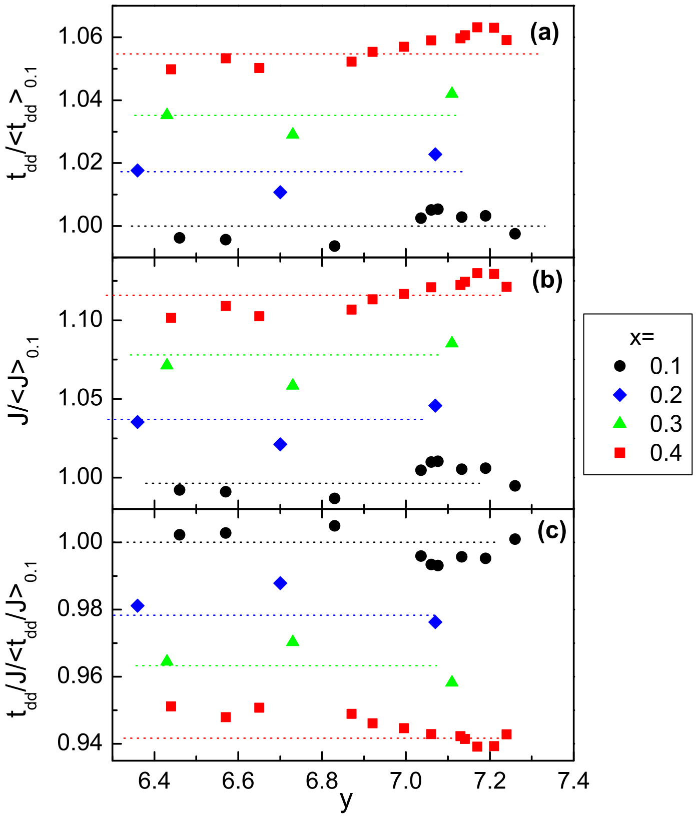

Figure 9.3: (a) The hopping rate t_{dd}, and (b) the superexchange coupling J calculated from Eq. (9.6) and (9.8), using the parameters shown in Fig. 9.2. (c) The ratio t_{dd}/J as a function of doping. The dotted lines are guides to the eye. All data sets are normalized to the $x = 0.1$ familiy.

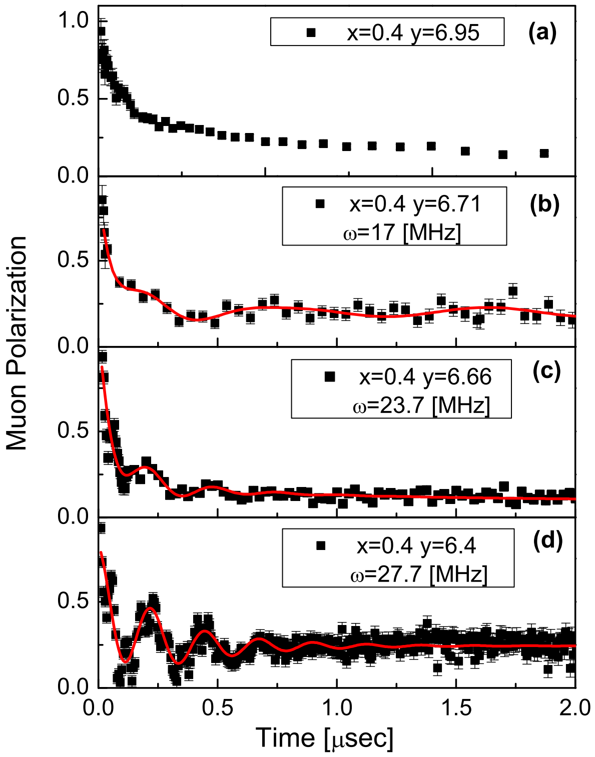

Figure 9.4: Raw muon polarization data and fits to Eq. 9.9 for four samples from the $x = 0.4$ family

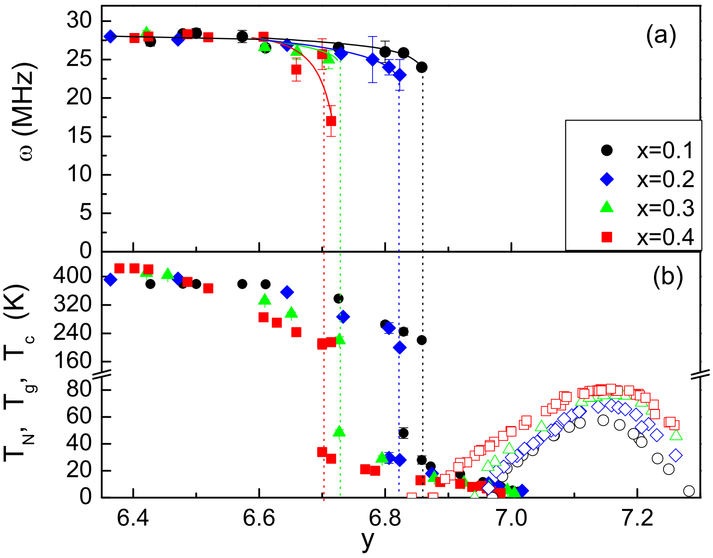

Figure 9.5: (a) The zero temperature muon oscillation frequency ω as a function of the chemical doping y for all four of the $(Ca_xLa_{1-x})(Ba_{1.75-x}La_{0.25+x})Cu_3O_y$ (CLBLCO) families. The antiferromagnetic zero temperature order parameter M_0 is proportional to ω. (b) The CLBLCO phase diagram as shown in section 7.1

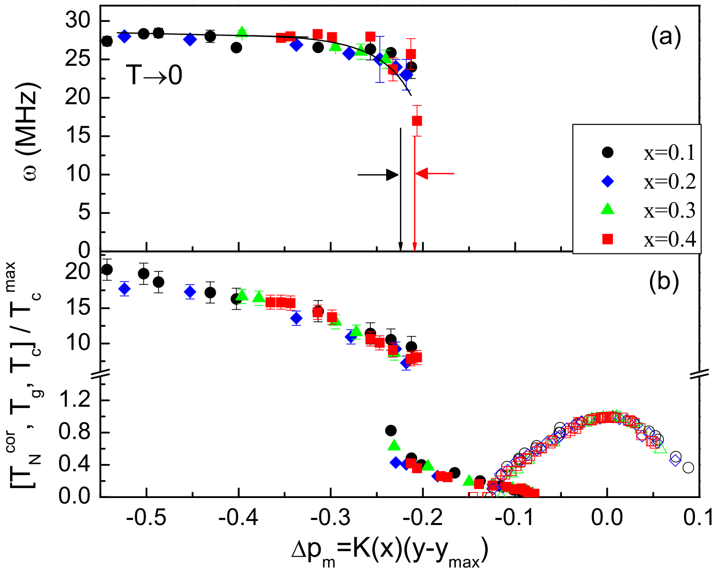

Figure 9.6: (a) The zero temperature muon oscillation frequency as a function of Δp_m for all four CLBLCO families; an equivalent to the staggered magnetization M_0 versus mobile hole density. The arrows show the expected variation of the critical doping from a 5% variation in t/J. (b) The CLBLCO phase diagram after scaling. as shown in chapter 8

Chapter 10

Discussion and Conclusions

In section 9.1 we showed, using structural considerations, that the ratio t/J is expected to change by $\backsim$5% between the $x = 0.1$ and $x = 0.4$ CLBLCO families.
In section 9.2 we discuss the plot of the AFM order parameter at zero temperature as a function of hole doping. This plot, and in particular the AFM critical doping, is determined by the ratio t/J (as discussed in chapter 6). However, Fig. 9.6(a) shows that the order parameter and the AFM critical doping is **family-independent** for the CLBLCO system. To demonstrate this point we show, using the two arrows in Fig. 9.6(a), what should have been the difference in the critical doping had it been proportional to t/J, and changed between the $x = 0.1$ and $x = 0.4$ by 5% (of 0.3). Thus, we conclude that $M_0(x, \Delta p_m)$ is x-independent, hence independent of t/J.

The above conclusion could, *a priori*, depend on the choice of the scaling parameters K's and y_{max}. A different set of K's or y_{max} would shift the magnetic critical doping with respect to each other. However, it will also shift the normalized T_c domes, T_g line, and T_N^{cor} line with respect to each other. We have attempted to use a different set of K's and y_{max}'s, which will not noticeably destroy the scaling of the normalized critical temperatures. We could not generate a variation of more than 2% in the M_0 critical doping. In other words, the different sets of K's and y_{max}'s always kept the critical doping well between the two vertical arrows in Fig. 9.6(c).

As mentioned in chapter 6, there are theoretical calculations in the limit of low doping, which show that t is renormalized downward from its bare value to an effective value J [49][50][51][52]. Our result could be explained by this theory, meaning that. This possibility could solve a profound riddle in the study of the CLBLCO system. This system was found to obey the Uemura relation $T_c \propto n_s$ [72], where n_s is the superconducting carrier density, in both under- and overdoped regions [73]. At the same time T_c^{max} scales with J as indicated before. Therefore, the Uemura relation should be rewritten as $T_c \propto Jn_s$. What is then the role of t? Our finding that the magnetic order parameter versus doping is universal suggests that at low temperature t and J unite.

Another plausible line of interpretation may be that different values of t/J correspond to different values of K, namely, the changes in t/J are canceled out by re-scales the doping axis. We currently do not have enough information on the origin of the scaling factor K to determine if that explanation is possible. However, we notice that K changes by up to 60% between the CLBLCO families. We find it hard to believe that such a significant difference in K will cancel out the difference much smaller difference in t/J.

An alternative explanation is that the destruction of the AFM order parameter is not a result of single holes hopping and should be described by a completely different Hamiltonian; perhaps hopping of boson pairs [74].

To conclude, an estimate of t and J from simple structure considerations using neutron diffraction shows that the origin of the different energy scales between the

CLBLCO families is mainly the different buckling angles. The difference in t/J between the two extreme families is about 5%. Although this is not an accurate way to measure the hopping rate or superexchange coupling, it does set the scale for the expected variation in the AFM critical doping. Using μSR, the AFM order parameter as a function of oxygen was determined for different families of the CLBLCO system. We used a scaling transformation to move from oxygenation level to mobile holes. Our measurements show that, at zero temperature, the order parameter as a function of mobile holes is independent of t/J within the required accuracy.

Appendix A

Derivation of the NQR Hamiltonian

The interaction energy of a charge density $\rho(r)$ with an electric potential V is:

$$E = \int \rho(r) V(r) dr. \tag{A.1}$$

Expanding $V(r)$ in a Taylor series and substituting it into (A.1) yields:

$$E = V(0) \int \rho dr + \sum_{\alpha} V_{\alpha} \int r_{\alpha} \rho dr + \frac{1}{2} \sum_{\alpha,\beta} V_{\alpha,\beta} \int r_{\alpha} r_{\beta} \rho dr \tag{A.2}$$

where $V_{\alpha} = \frac{\partial V}{\partial r_{\alpha}}|_{r=0}$ and $V_{\alpha\beta} = \frac{\partial^2 V}{\partial r_{\alpha} \partial r_{\beta}}|_{r=0}$.

Since the nucleus is the center of mass, the first term is the electric monopole, the electrostatic energy of the nucleus. The second term is the interaction of the electric dipole moment of the nucleus with the electric field. This term vanishes since in the center of mass frame the electric dipole moment is zero. The third term is the quadruple interaction. $V_{\alpha\beta}$ is called the Electric Field Gradient (EFG) tensor.

A.0.1 The EFG

In the quadrupole interaction the environment is taken into account by the EFG. The EFG reflects the asymmetry in the nucleus environment. The principal axes can always be chosen so that $V_{\alpha\beta} = 0$ for $\alpha \neq \beta$ so a diagonal EFG tensor can be written: $V = \begin{pmatrix} V_{XX} & 0 & 0 \\ 0 & V_{YY} & 0 \\ 0 & 0 & V_{zz} \end{pmatrix}$ the directions are defined by:$|V_{XX}| \leq |V_{YY}| \leq |V_{ZZ}|$

From the Laplace equation: $\nabla^2 V = 0 \Rightarrow V_{XX} + V_{YY} + V_{ZZ} = 0$. Therefore the number of parameters can be reduced and the EFG tensor can be written as:

$$V = \begin{pmatrix} -\frac{1-\eta}{2} & 0 & 0 \\ 0 & -\frac{1+\eta}{2} & 0 \\ 0 & 0 & 1 \end{pmatrix}. \tag{A.3}$$

where: $eq = V_{zz}$ and $\eta = \frac{V_{YY} - V_{XX}}{V_{ZZ}}$ is the asymmetry parameter.

A.0.2 The quadrupole tensor of the nucleus

The quadrupole tensor is defined as:

$$Q_{\alpha\beta} = \int (3r_\alpha r_\beta - \delta_{\alpha\beta} r^2)\rho dr. \tag{A.4}$$

The quadrupole energy can be written as

$$E_q = \frac{1}{6} \sum_{\alpha,\beta} V_{\alpha\beta} Q_{\alpha\beta}, \tag{A.5}$$

since the term $V_{\alpha\beta}\delta_{\alpha\beta} \int r^2 \rho dr$ is zero from the Laplace equation.

A.0.3 Quantum mechanical treatment

For a quantum mechanical expression we replace the charge density with the operator $\rho^{(op)}(r) = e\sum\limits_{k}\delta(r - r_k)$, where k - proton number, and hence

$$Q^{(op)}_{\alpha,\beta} = e\sum_{k}(3r_{\alpha k}r_{\beta k} - \delta_{\alpha\beta}r_k^2). \tag{A.6}$$

And the Hamiltonian:

$$\mathcal{H}_Q = \frac{1}{6}\sum_{\alpha,\beta}V_{\alpha\beta}Q^{(op)}_{\alpha\beta}. \tag{A.7}$$

The eigenstates of the nucleus are characterized by the total angular momentum I of each state, $2I+1$ values of the z component of the angular momentum, and a set of other quantum number ς. Since we are only interested in the spatial reorientation of the nucleus for a given nuclear energy state, we only need the matrix elements diagonal in both I and ς: $\left\langle \mathrm{I}M\zeta \left| Q^{(op)}_{\alpha\beta} \right| IM'\zeta \right\rangle$.

This expression contains the matrix elements of the coordinates operators. Since for each nucleus its location is connected to its orbital angular momentum, for example: $l_X = \frac{1}{i}\left(y\frac{d}{dz} - z\frac{d}{dy}\right)$, we can convert the coordinates operators to the angular momentum operators. x, y, z refer to the principal directions of the EFG. I_x,I_y,I_z are the operators of the total angular momentum of the nucleus: $I_x = \sum_k l_{xk} + S_{xk}$ etc..., where l_{xk} and S_{xk} are the x components of the orbital and spin angular momentum of the k-th nucleon.

We now use the irreducible tensor operators T_{2M} [33]. Since the term $3r_{\alpha k}r_{\beta k} - \delta_{\alpha\beta}r_k^2$ is a linear combination of these operators, We replace the coordinates operators with the angular momentum operators, by replacing $(x+iy)$ with I^+, $(x-iy)$ with I^- and z with I_z, to get the T_{2M} constructed from I^+, I^- and I_z.

We now use the Wigner-Eckhart theorem [75] that states:

$$\langle \mathrm{I}M\zeta \left| T_{LM} \right| I'M'\zeta' \rangle = C\, \langle I\zeta \left| T_L \right| I'\zeta' \rangle \tag{A.8}$$

where C is a constant.

It can be shown [33] that using this theorem we obtain:

$$\left\langle \mathrm{I}M\zeta \left| e\sum_k (3r_{\alpha k}r_{\beta k} - \delta_{\alpha\beta}r_k^2) \right| IM'\zeta \right\rangle = C\left\langle \mathrm{I}M\zeta \left| 3\frac{(I_\alpha I_\beta + I_\beta I_\alpha)}{2} - \delta_{\alpha\beta}I^2 \right| IM'\zeta \right\rangle . \tag{A.9}$$

so the Hamiltonian can be written as:

$$\mathcal{H}_Q = \frac{\hbar \upsilon_q}{6}\left[3I_Z^2 - I^2 + \eta\left(I_X^2 - I_Y^2\right)\right] \tag{A.10}$$

where: $\upsilon_q \equiv \frac{3e^2qQ}{2I(2I-1)\hbar}$, $eq = V_{zz}$

and the quadrupole moment of the nucleus is: $Q = \frac{1}{e}\left\langle I, m \left| \sum_k 3Z_k^2 - r_k^2 \right| I, m \right\rangle$.

For spin $\frac{3}{2}$ the standard basis is

$$\begin{aligned} \langle 3/2| &= \begin{pmatrix} 1 & 0 & 0 & 0 \end{pmatrix} & \langle 1/2| = \begin{pmatrix} 0 & 1 & 0 & 0 \end{pmatrix} \\ \langle -1/2| &= \begin{pmatrix} 0 & 0 & 1 & 0 \end{pmatrix} & \langle -3/2| = \begin{pmatrix} 0 & 0 & 0 & 1 \end{pmatrix} \end{aligned} \tag{A.11}$$

$$\hat{\mathbf{I}} = \left[\begin{pmatrix} 0 & \frac{\sqrt{3}}{2} & 0 & 0 \\ \frac{\sqrt{3}}{2} & 0 & 1 & 0 \\ 0 & 1 & 0 & \frac{\sqrt{3}}{2} \\ 0 & 0 & \frac{\sqrt{3}}{2} & 0 \end{pmatrix}, \begin{pmatrix} 0 & -i\frac{\sqrt{3}}{2} & 0 & 0 \\ i\frac{\sqrt{3}}{2} & 0 & -i & 0 \\ 0 & i & 0 & -i\frac{\sqrt{3}}{2} \\ 0 & 0 & i\frac{\sqrt{3}}{2} & 0 \end{pmatrix}, \begin{pmatrix} 3/2 & 0 & 0 & 0 \\ 0 & 1/2 & 0 & 0 \\ 0 & 0 & -1/2 & 0 \\ 0 & 0 & 0 & -3/2 \end{pmatrix}\right] \tag{A.12}$$

and the matrix representation of A.10 in this basis is

$$\mathcal{H}_Q = \frac{\omega_0\hbar}{6}\begin{pmatrix} 3 & 0 & \eta\sqrt{3} & 0 \\ 0 & -3 & 0 & \eta\sqrt{3} \\ \eta\sqrt{3} & 0 & -3 & 0 \\ 0 & \eta\sqrt{3} & 0 & 3 \end{pmatrix} \tag{A.13}$$

Diagonal form of the Hamiltonian

The matrix that diagonalizes $\mathcal{H}_Q$ is

$$T = \frac{1}{\sqrt{1+\sigma^2}} \begin{pmatrix} 1 & 0 & \sigma & 0 \\ 0 & 1 & 0 & -\sigma \\ -\sigma & 0 & 1 & 0 \\ 0 & \sigma & 0 & 1 \end{pmatrix} \tag{A.14}$$

Where ς and σ are defined as

$$\sigma \triangleq \frac{\eta}{\sqrt{3}(1+\varsigma)} \quad , \quad \varsigma \triangleq \sqrt{1+\frac{\eta^2}{3}} \tag{A.15}$$

And the diagonal form is

$$\mathcal{H}_Q^{diagonal} = T\mathcal{H}_Q T^{\dagger} = \frac{\omega_0 \hbar \varsigma}{2} \begin{pmatrix} 1 & 0 & 0 & 0 \\ 0 & -1 & 0 & 0 \\ 0 & 0 & -1 & 0 \\ 0 & 0 & 0 & 1 \end{pmatrix} \tag{A.16}$$

We therefore conclude that our system is composed of two doublets of energy.

$$E_{1,2} = (\omega_0/2)(1+\eta^2/3)^{1/2} \tag{A.17}$$

$$E_{3,4} = -(\omega_0/2)(1+\eta^2/3)^{1/2}$$

and, $2\pi f_{NQR} = \omega_0(1+\eta^2/3)^{-1/2}$ is the resonance frequency.

Appendix B

Interaction with an external time dependent magnetic field

In this Appendix we add to the NQR Hamiltonian an interaction with an external time dependent magnetic field. Since the reference frame of the problem is defined by the three principal axes of the EFG tensor, orienting the coil in an arbitrary direction of space yields a magnetic field of the form

$$\mathbf{B}(t) = 2B_1 \cos(\omega t)\,[\sin(\theta)\cos(\phi), \sin(\theta)\sin(\phi), \cos(\theta)] \tag{B.1}$$

This field defines another characteristic frequency in the system

$$\omega_1 \triangleq \gamma B_1 \tag{B.2}$$

and the Hamiltonian becomes $\mathcal{H}(t) = \mathcal{H}_Q + \hat{W}(t)$ with

$$\begin{aligned} \hat{W}(t) = \hbar\gamma B_1 \cdot I &= 2\hbar\omega_1 \cos(\omega t)\cos(\theta) \begin{pmatrix} \frac{3}{2} & 0 & 0 & 0 \\ 0 & \frac{1}{2} & 0 & 0 \\ 0 & 0 & -\frac{1}{2} & 0 \\ 0 & 0 & 0 & -\frac{3}{2} \end{pmatrix} \\ &+2\hbar\omega_1 \cos(\omega t)\sin(\theta) \begin{pmatrix} 0 & \frac{\sqrt{3}}{2}e^{-i\phi} & 0 & 0 \\ \frac{\sqrt{3}}{2}e^{i\phi} & 0 & e^{-i\phi} & 0 \\ 0 & e^{i\phi} & 0 & \frac{\sqrt{3}}{2}e^{-i\phi} \\ 0 & 0 & \frac{\sqrt{3}}{2}e^{i\phi} & 0 \end{pmatrix} \end{aligned} \tag{B.3}$$

Since we've transformed $\mathcal{H}_Q$ to a diagonal form we must apply the same transformation to the perturbation part ($\hat{W}^{diagonal}(t) = T\hat{W}(t)T^{\dagger}$), a calculation that ends with

$$\begin{aligned} \hat{W}^{diagonal}(t) &= \frac{2\hbar\omega_1 \cos(\omega t)}{1+\sigma^2}\cos(\theta) \begin{pmatrix} \frac{3}{2}-\frac{\sigma^2}{2} & 0 & -2\sigma & 0 \\ 0 & \frac{1}{2}-\frac{3\sigma^2}{2} & 0 & 2\sigma \\ -2\sigma & 0 & -\frac{1}{2}+\frac{3\sigma^2}{2} & 0 \\ 0 & 2\sigma & 0 & -\frac{3}{2}+\frac{\sigma^2}{2} \end{pmatrix} \\ &+\frac{2\hbar\omega_1 \cos(\omega t)}{1+\sigma^2}\sin(\theta) \begin{pmatrix} 0 & D^* & 0 & F^* \\ D & 0 & E^* & 0 \\ 0 & E & 0 & D^* \\ F & 0 & D & 0 \end{pmatrix} \end{aligned} \tag{B.4}$$

Where D, E and F are defined as

$$\begin{aligned} D &\triangleq \frac{\sqrt{3}}{2}e^{i\phi}\left[1-\sigma^2+\frac{2}{\sqrt{3}}\sigma e^{-2i\phi}\right] \triangleq D_0 e^{i\lambda} \\ E &\triangleq e^{i\phi}\left[1-\sigma\sqrt{3}e^{-2i\phi}\right] \\ F &\triangleq \frac{\sqrt{3}}{2}e^{i\phi}\left[2\sigma+\frac{2}{\sqrt{3}}\sigma^2 e^{-2i\phi}\right] \end{aligned} \tag{B.5}$$

Since $\frac{\omega_0}{\omega_1} \approx 100$ the diagonal elements of Eq. (B.4) are much smaller than those of Eq. (A.16) and we omit them. Furthermore, according to the off resonance approximation we can also omit the terms with E and F since a time dependent perturbation can not couple degenerate energy levels. Our Hamiltonian is thus reduced to

$$\begin{aligned}
\hat{H}^{diagonal}(t) &= \frac{\omega_0 \hbar \varsigma}{2} \begin{pmatrix} 1 & 0 & 0 & 0 \\ 0 & -1 & 0 & 0 \\ 0 & 0 & -1 & 0 \\ 0 & 0 & 0 & 1 \end{pmatrix} + \\
& \frac{2\hbar\omega_1 D_0 \cos(\omega t)}{1+\sigma^2} \begin{pmatrix} 0 & e^{-i\lambda}\sin(\theta) & -\frac{2\sigma}{D_0}\cos(\theta) & 0 \\ e^{i\lambda}\sin(\theta) & 0 & 0 & \frac{2\sigma}{D_0}\cos(\theta) \\ -\frac{2\sigma}{D_0}\cos(\theta) & 0 & 0 & e^{-i\lambda}\sin(\theta) \\ 0 & \frac{2\sigma}{D_0}\cos(\theta) & e^{i\lambda}\sin(\theta) & 0 \end{pmatrix}
\end{aligned}$$

By using the definitions of Eq. (B.5), (A.15) and the following new ones

$$\mathbf{a} \triangleq \frac{1}{2\sqrt{3+\eta^2}} (\eta+3, \eta-3, 2\eta) \tag{B.6}$$

$$A_{\pm} \triangleq a_x \cos(\phi) \pm i a_y \sin(\phi) \quad , \quad A_z \triangleq a_z \tag{B.7}$$

$$\epsilon \triangleq \sqrt{A_+ A_- \sin^2(\theta) + A_z^2 \cos^2(\theta)} \tag{B.8}$$

$\hat{H}^{diagonal}(t)$ can be written in a more convenient way

$$\hat{H}^{diagonal}(t) = \frac{\omega_0 \hbar \varsigma}{2} \begin{pmatrix} 1 & 0 & 0 & 0 \\ 0 & -1 & 0 & 0 \\ 0 & 0 & -1 & 0 \\ 0 & 0 & 0 & 1 \end{pmatrix} + 2\hbar\omega_1 \cos(\omega t) \begin{pmatrix} 0 & A_+ \sin(\theta) & -A_z \cos(\theta) & 0 \\ A_- \sin(\theta) & 0 & 0 & A_z \cos(\theta) \\ -A_z \cos(\theta) & 0 & 0 & A_+ \sin(\theta) \\ 0 & A_z \cos(\theta) & A_- \sin(\theta) & 0 \end{pmatrix} \tag{B.9}$$

Note that for $\eta = 0$, $A_z = 0$, and the Hamiltonian becomes:

$$\hat{H}^{diagonal}(t)(\eta = 0) = \frac{\omega_0 \hbar \varsigma}{2} \begin{pmatrix} 1 & 0 & 0 & 0 \\ 0 & -1 & 0 & 0 \\ 0 & 0 & -1 & 0 \\ 0 & 0 & 0 & 1 \end{pmatrix} + 2\hbar\omega_1 \cos(\omega t) \begin{pmatrix} 0 & A_+ \sin(\theta) & 0 & 0 \\ A_- \sin(\theta) & 0 & 0 & 0 \\ 0 & 0 & 0 & A_+ \sin(\theta) \\ 0 & 0 & A_- \sin(\theta) & 0 \end{pmatrix} \tag{B.10}$$

In this case when transmitting in the $\hat{z}$ direction ($\theta = 0$), there are no off-diagonal terms left, and there will be no transitions.

References

[1] M. Vershinin, S. Misra, S. Ono, Y. Abe, Y. Ando, and A. Yazdani, *Science* **303**, 1995 (2004).

[2] A. J. Vega, *Israel Journal of Chemistry* **32**, 195 (1992).

[3] R. Ofer, *Ms.C thesis, Thechnion - Israel Institute of Technology* (2004).

[4] D. Yamamoto and S. Kurihara, *Phys. Rev. B* **75**, 134520 (2007).

[5] O. Chmaissem, J. D. Jorgensen, S. Short, A. Knizhnik, Y. Eckstein, and H. Shaked, *Nature* **397**, 45 (1999).

[6] A. Montorsi, *cond-mat* **0804.3284** (2008).

[7] E. Arrigoni, E. Fradkin, and S. A. Kivelson, *Phys. Rev. B* **69**, 214519 (2004).

[8] M. Capone, G. Sangiovanni, C. Castellani, C. D. Castro, and M. Grilli, *Phys. Rev. Lett.* **92**, 106401 (2004).

[9] U. Low, V. J. Emery, K. Fabricius, and S. A. Kivelson, *Phys. Rev. B* **72**, 1918 (1994).

[10] S. A. Kivelson, I. P. Bindloss, E. Fradkin, V. Oganesyan, J. M. Tranquada, A. Kapitulnik, and C. Howald, *Rev. Mod. Phys.* **75**, 1201 (2003).

[11] M. Aichhorn, E. Arrigoni, M. Potthoff, and W. Hanke, *Phys. Rev. B* **76**, 224509 (2007).

[12] V. J. Emery, S. A. Kivelson, and O. Zachar, *Phys. Rev. B* **56**, 6120 (1997).

[13] P. M. Singer, A. W. Hunt, and T. Imai, *Phys. Rev. Lett* **88**, 047602 (2002).

[14] K. Yamada, C. H. Lee, K. Kurahashi, J. Wada, S. Wakimoto, S. Ueki, H. Kimura, Y. Endoh, S. Hosoya, G. Shirane, R. J. Birgeneau, M. Greven, M. A. Kastner, and Y. J. Kim, *Phys. Rev. B* **57**, 6165 (1998).

[15] C. Niedermayer, C. Bernhard, T. Blasius, A. Golnik, A. Moodenbaugh, and J. Budnick, *Phys. Rev. Lett.* **80**, 3843 (1998).

[16] C. Panagopoulos, J. L. Tallon, B. D. Rainford, T. Xiang, J. R. Cooper, and C. A. Scott, *Phys. Rev. B* **66**, 064501 (2002).

[17] K. McElroy, R. W. Simmonds, J. E. Hoffman, D.-H. Lee, J. Orenstein, H. Eisaki, S. Uchida, and J. C. Davis, *Nature* **422**, 592 (2003).

[18] K. M. Lang, V. Madhavan, J. E. Hoffman, E. W. Hudson, H. Eisaki, S. Uchida, and J. C. Davis, *Nature* **415**, 412 (2002).

[19] J. E. Hoffman, K. McElroy, D.-H. Lee, K. M. Lang, H. Eisaki, S. Uchida, and J. C. Davis, *Science* **297**, 1148 (2002).

[20] H. A. Mook, P. Dai, and F. Dogan, *Phys. Rev. Lett.* **88**, 097004 (2002).

[21] S. Sanna, G. Allodi, G. Conacas, A. D. Hillier, and R. D. Renzi, *Phys. Rev. Lett.* **93**, 207001 (2004).

[22] R. I. Miller, R. F. Kiefl, J. H. Brewer, F. D. Callaghan, J. E. Sonier, R. Liang, D. A. Bonn, and W. Hardy, *Phys. Rev. B* **73**, 144509 (2006).

[23] J. Bobroff, H. Alloul, S. Ouazi, P. Mendels, A. Mahajan, N. Blanchard, G. Collin, V. Guillen, and J. F. Marucco, *Phys. Rev. Lett.* **89**, 157002 (2002).

[24] H. a. Mook, Y. Sidis, B. Fauque, V. Baledent, and P. Bourges, *cond-mat* **0802.3620** (2008).

[25] H. L. Edwardsand, D. J. Derro, A. L. Barr, J. T. Markert, and A. L. de Lozanne, *Phys. Rev. Lett.* **75**, 1387 (1995).

[26] N. C. Yeh, C.-T. Chen, G. Hammerl, J. Mannhart, A. Schmehl, C. W. Schneider, R. R. Schulz, S. Tajima, K. Yoshida, D. Garrigus, and M. Strasik, *Phys. Rev. Lett.* **87**, 087003 (2001).

[27] J. M. Tranquada, D. E. Cox, W. Kunnmann, H. Moudden, G. Shirane, M. Suenaga, P. Zolliker, D. Vaknin, S. K. Sinha, M. S. Alvarez, A. J. Jacobson, and D. C. Johnston, *Phys. Rev. Lett.* **60**, 156 (1988).

[28] A. Knizhnik, *Journal of Physics and Chemistry of Solids* **64**, 273 (2003).

[29] A. J. Vega, W. E. Farneth, E. M. McCarron, and R. K. Bordia, *Phys. Rev. B* **39**, 2322 (1989).

[30] H. Yasuoka, T. Shimiza, Y. Ueda, and K. Kosuge, *Journal of the Physical Society of Japan* **57**, 2659 (1988).

[31] C. H. Pennington, D. J. Durand, D. B. Zax, C. P. Slichter, J. P. Rice, and D. M. Ginsberg, *Phys. Rev. B* **37**, 7944 (1988).

[32] H. Lutgemeier, *Physica C* **153**, 95 (1988).

[33] C. P. Slichter, *Principles of Magnetic Resonance, Third edition. Springer-Verlag,Springer-Verlag* (1990).

[34] J. F. Baugher, P. C. Taylor, T. Oja, and P. J. Bray, *J. Chem. Phys.* **50**, 4914 (1969).

[35] T. P. Das and E. L. Hahn, *Nuclear Quadrupole Resonance Spectroscopy, Academic Press INC, New York* (1958).

[36] T. Shimizu, H. Yasuoka, T. Imai, T. Tsuda, T. Takabatake, Y. Nakazawa, and M. Ishikawa, *Journal of the Physical Society of Japan* **57**, 2494 (1988).

[37] K. Schwarz, C. Ambrosch-Draxl, and P. Blaha, *Phys. Rev. B* **42**, 2051 (1990).

[38] G. S. Harbison, A. Solkenbergs, and T. M. Barbara, *J. Chem. Phys.* **90**, 5292 (1989).

[39] G. S. Harbison and A. Solkenbergs, *Z. Naturforsch* **45a**, 575 (1990).

[40] J. C. Pratt, P. Raganuthan, and C. A. McDowell, *J. Magn. Reson.* **20**, 313 (1975).

[41] S. Levy and A. Keren, *Journal of Magnetic Resonance* **167**, 317 (2004).

[42] K. McElroy, J. Lee, J. A. Slezak, D.-H. Lee, H. Eisaki, S. Uchida, and J. C. Davis, *Science* **309**, 1048 (2005).

[43] T. S. Nunner, P. J. Hirschfeld, B. M. Andersen, A. Melikyan, and K. McElroy, *cond-mat* **0606685** (2006).

[44] M. Mori, G. Khaliullin, T. Tohyama, and S. Maekawa, *cond-mat* **0805.1281** (2008).

[45] P. W. Anderson, *science* **235**, 1196 (1987).

[46] F. C. Zang and T. Rice, *Phys. Rev. B* **37**, 3759 (1988).

[47] E. Dagotto, *Rev. Mod. Phys.* **66**, 763 (1994).

[48] P. A. Lee, N. Nagaosa, and X. G. Wen, *Rev. Mod. Phys.* **78**, 17 (2006).

[49] S. Schmitt-Rink, C. Varma, and A. E. Ruckenstein, *Phys. Rev. Lett.* **60**, 2793 (1988).

[50] C. L. Kane, P. A. Lee, and N. Read, *Phys. Rev. B* **39**, 6880 (1989).

[51] Z. Liu and E. Manousakis, *Phys. Rev. B* **45**, 2425 (1992).

[52] E. Altman and A. Auerbach, *Phys. Rev. B* **65**, 104508 (2002).

[53] G. Khaliullin and P. Horsch, *Phys. Rev. B* **47**, 463 (1993).

[54] A. Belkasri and J. L. Richard, *Phys. Rev. B* **50**, 12896 (1994).

[55] J. L. Richard and V. Y. Yushankhaï, *Phys. Rev. B* **50**, 12927 (1994).

[56] D. Goldschmidt, G. M. Reisner, A. K. Y. Direktovitch and, E. Gartstein, G. Kimmel, and Y. Eckstein, *Phys. Rev. B* **48**, 532 (1993).

[57] S. Marchand, *Ph. D. thesis, Universite Paris 6* .

[58] A. Keren, A. Kanigel, and G. Bazalitsky, *Phys. Rev. B* **74**, 172506 (2006).

[59] R. Ofer, G. Bazalitsky, A. Kanigel, A. Keren, A. Auerbach, J. S. Lord, and A. Amato, *Phys. Rev. B* **74**, 220508(R) (2006).

[60] A. Kanigel, A. Keren, Y. Eckstein, A. Knizhnik, J. S. Lord, and A. Amato., *Phys. Rev. Lett.* **88**, 137003 (2002).

[61] H. M. Rietvelt, *Journal of Applied Crystallography* **2**, 65 (1969).

[62] C. Larson and R. B. V. Dreele, *Los Alamos National Laboratory* (1994).

[63] B. H. Toby, *Journal of Applied Crystallography* **34**, 210 (2001).

[64] D. P. Arovas and A. Auerbach, *Phys. Rev. B* **38**, 316 (1988).

[65] B. Keimer, A. Aharony, A. Auerbach, R. J. Birgeneau, A. Cassanho, Y. Endoh, R. W. Erwin, M. A. Kastner, and G. Shirane, *Phys. Rev. B* **45**, 7430 (1992).

[66] M. Abramovitz and I. A. Stegun, *Handbook of Mathenatical Functions, Dover Publications, Inc. New York* (1970).

[67] E. Pavarini, I. Dasgupta, T. Saha-Dasgupta, O. Jepsen, and O. K. Andersen, *Phys. Rev. Lett.* **87**, 047003 (2001).

[68] J. Zaaneann and D. G. A. Sawatzky, *Can. J. Phys.* **65**, 1262 (1987).

[69] W. A. Harrison, *Electronic Structure and the Properties of Solids, W. H. Freeman and company, San Fransisco* (1980).

[70] M.-B. Lepetit, *In preparation* .

[71] A. Keren, L. P. Le, G. M. Luke, B. J. Sternlieb, W. D. Wu, Y. J. Uemura, S. Tajima, and S. Uchida, *Phys. Rev. B* **48**, 12926 (1993).

[72] Y. J. Uemura, G. M. Luke, B. J. Sternlieb, J. H. Brewer, J. F. Carolan, W. N. Hardy, R. Kadono, J. R. Kempton, R. F. Kiefl, S. R. Kreitzman, P. Mulhern, T. M. Riseman, D. L. Williams, B. X. Yang, S. Uchida, H. Takagi, J. Gopalakrishnan, A. W. Sleight, M. A. Subramanian, C. L. Chien, M. Z. Cieplak, G. Xiao, V. Y. Lee, B. W. Statt, C. E. Stronach, W. J. Kossler, , and X. H. Yu, *Phys. Rev. Lett.* **62**, 2317 (1989).

[73] A. Keren, A. Kanigel, J. S. Lord, and A. Amato, *Solid State Commun.* **126**, 39 (2003).

[74] M. Havilio and A. Auerbach, *Phys. Rev. Lett.* **83**, 4848 (1999).

[75] C. Tannoudji, B. Diu, and F. Laloe, *Quantum Mechanics, Vol 2, page 1048* .

איתור חוסר הומוגניות במטען ומעבר לסדר מגנטי בעל מוליכים נחושתיים

רינת עופר

איתור חוסר הומוגניות במטען ומעבר לסדר מגנטי בעל מוליכים נחושתיים

חיבור על מחקר

לשם מילוי חלקי של הדרישות לקבלת תואר
דוקטור לפילוסופיה

רינת עופר

הוגש לסנט הטכניון — מכון טכנולוגי לישראל
אלול תשס"ח　　　　חיפה　　　　ספטמבר 2008

חיבור על מחקר נעשה בהדרכת עמית קרן

בפקולטה לפיסיקה

הכרת תודה

אני מודה לטכניון על התמיכה הכספית הנדיבה בהשתלמותי

תקציר

מוליכי העל הנחושתיים הם תרכובות קרמיות המכילות מישורים של נחושת וחמצן, הניתנים לסימום על ידי הכנסת חורים טעונים. הכנסת החורים מתבצעת ע״י החלפת אטומים מחוץ למישורים באטומים אחרים בעלי מספר שונה של אלקטרונים ברמה החיצונית. ניתן להסתכל על חומרים אלה כתלות ברמת הסימום: ברמות סימום נמוכות מאוד חומרים אלה הם מבודדים אנטיפרומגנטים. עם עלית רמת הסימום, טמפרטורת המעבר למצב אנטיפרטומגנט T_N יורדת מהר מאוד, עד שברמת סימום של בערך 4% אין יותר סדר מגנטי לטווח ארוך. מעל רמת סימום מסוימת מופיעה העל מוליכות. טמפרטורת המעבר למצב על מוליך T_C עולה עם הסימום עד לרמה של סימום אופטימלי שבו טמפרטורת המעבר היא מכסימלית. סימום נוסף מעבר לרמה זו גורם לירידה ב T_N.

עבודה זו בנויה משני חלקים שונים. החלק הראשון עוסק במדידה של חוסר הומוגניות במטען במישורי ה - CuO_2 של התרכובת העל מוליכה $YBa_2Cu_3O_y(YBCO)$. המדידות נעשו עבור דגמים בעלי רמות סימום שונות בתחום הפאזה העל מוליכה בדיאגרמת הפאזות. אחת משאלות המפתח בתחום של העל מוליכים הנחושתיים היא הקביעה האם חוסר ההומוגנית במטען, שהתגלה במספר מתרכובות אלו, הוא חלק הכרחי במנגנון העל מוליכות. עד היום, מדידות של אנאיזוטרופיה במישורים ב $YBCO$ נעשו רק ברמת הסימום האופטימאלית. מטרת החלק הזה של המחקר היא למדוד חוסר הומוגניות אפשרי במטען בדגמי $YBCO$ בעלי רמת סימום נמוכה יותר, ולראות האם יש קורלציה בין המבנה האלקטרוני של המישורים העל מוליכים ובין מיקום האטומים המשמשים לסימום הדגם. ניסוי

זה יאפשר לנו לומר האם מודלים תאורטים המנבאים חוסר הומוגניות והפרדת פאזות במישורים מבלי להביא בחשבון את האטומים המשמשים לסימום, הם אכן רלוונטיים לעל מוליכות בטמפרטורה גבוהה או לא.

למטרה זו ביצענו ניסויים של תהודה מגנטית גרעינית (NMR), ותהודה מגנטית קוודרפולית (NQR), בדגמי $YBCO$. במדידת NMR הפעלת שדה מגנטי חיצוני קבוע גורמת להפרדה בין רמות האנרגיה הגרעיניות. הפעלת שדה מגנטי תלוי בזמן בתדר הרזוננס בניצב לכיוון השדה הקבוע, מאלצת מעבר בין רמות האנרגיה. בגרעינים שהתפלגות המטען בהם אינה ספרית, כגון גרעין הנחושת בעל ספין 3/2, מומנט הקוודרופול החשמלי של המטענים הסובבים את הגרעין גורם להזזה של רמות האנרגיה וליצירת תדרי רזוננס נוספים. בניסוי NQR, אין שדה מגנטי קבוע, מומנט הקוודרופול החשמלי גורם ליצירת שתי רמות אנרגיה לגרעין. ההפרש בין רמות האנרגיה נקבע על ידי הנגזרות השניות של השדה החשמלי של המטענים הסובבים את הגרעין [EFG]. בניסוי NQR , בדומה לניסוי NMR, מודדים את תדר התהודה למעבר בין רמות האנרגיה. המדידה מתבצעת ע"י הפעלת פולסים של זרם חילופין בתדירות rf. הפולסים משודרים לסליל שבתוכו נמצא הדגם ויוצרים שדה בכיוון הציר של הסליל. כאשר תדירות השידור מתאימה לתדירות הרזוננס למעבר בין רמות האנרגיה, נוצר הד בסליל, הנמדד במערכת ע"י קביעת המתח בסליל. אחד הפרמטרים של ההמילטוניאן הקוודרופולי הוא פרמטר האנאיזוטרופיה שממנו ניתן ללמוד על איזוטרופית פיזור המטען סביב הגרעין.

המדידות בוצעו על גרעין הנחושת, כיוון שאנו מעוניינים מבנה האלקטרוני של המישורי ה- CuO_2. כדי לפשט את הספקטרום ולאפשר הבחנה טובה יותר בין אתרי הנחושת השונים, הדגמים בניסוי היו מועשרים באיזוטופ הנחושת ^{63}Cu. בעבודה זו אני משווים בין שלוש שיטות שונות למדידת פרמטר האנאיזוטרופיה. אנו משווים בין שיטה חדשה, הנקראת תהודה מגנטית קוודרופולית תלוית זווית ($ADNQR$), ובין שתי שיטות ותיקות יותר: ספקטרוסקופית $Nutation$, וניסוי NMR שגרתי.

ניסוי ה NMR הראה כי ניתן למדוד את פרמטר האנאיזוטרופיה רק ב $YBCO$ ברמת

סימום אופטימאלית. ברמות הסימום הנמוכות יותר קו ה NMR נעשה רחב וחלש ולא ניתן לקבוע באופן חד משמעי את תדירויות הרזוננס, ולכן לא ניתן לחלץ את פרמטר האנאיזוטרופיה מתוך הקו.

השילוב של ניסוי ה $Nutation$ וניסוי ה $ADNQR$ הראה כי ב $YBCO_7$, עבור הנחושת במישורים העל מוליכים פיזור המטען הוא איזוטרופי, תוצאה זו מתאימה למדידות NMR קודמות. בדגם בעל רמת סימום נמוכה יותר התקבלו תוצאות שונות עבור אתרים שונים של נחושת במישורים. עבור נחושת בסביבה זהה לזו שקיימת ב $YBCO_7$, התקבל כי פיזור המטען הוא איזוטרופי. לעומת זאת עבור נחושת שנמצאת בסביבה שבה יש חוסר באטומי חמצן המשמשים לסימום בשרשראות, ישנו חוסר הומוגניות במישורי ה CuO_2.

תוצאות הניסויים מלמדות כי חוסר הומוגניות במטען נמצא רק באתרים בהם יש חוסר של אטומי חמצן בשרשראות. כלומר אם קיימת הפרדת פאזות במישורים העל מוליכים בתרכובת זו, היא קשורה באטומי החמצן המשמשים לסימום, ולכן לא יכולה להיות תכונה של המישורים עצמם.

החלק השני של העבודה מתרכז ברמות סימום נמוכות יותר, באזור בדיאגרמת הפאזות שבו יש מעבר מאי הומוגניות לסדר מגנטי. בחלק זה המדידות נעשו בעזרת $muSR$ (סיבוב של ספין המיואון). בשיטה זו מיואונים מוחדרים לתוך הדגם, כך שהספין של כל המיואונים מקוטב באותו כיוון, בניגוד לכיוון התנועה של האלומה. ברגע שהמיואון עוצר בתוך הדגם הספין שלו מבצע פרסציה סביב השדה המגנטי המקומי שהוא חש, כאשר תדר הסיבוב נקבע על פי גודל השדה. זמן החיים של המיואון הוא כ-2.2 מיקרושניה. הוא דועך לפוזיטרון ושני ניטרינו. עקב אי- הסימטריה של הכוח החלש הפוזיטרון נפלט בעדיפות בכיוון הספין של המיאון ברגע הדעיכה. הדגם מוקף במספר גלאי פוזיטרונים שמאפשרים לעקוב אחר הקיטוב הממוצע של המיואונים כתלות בזמן, ומכאן לשחזר את התפלגות השדה המגנטי בתוך הדגם. תדירות הסיבוב של המיואון בדגם פרופורציונית לשדה הפנימי שאותו הוא חש ומכאן ניתן למדוד את פרמטר הסדר האנטיפרומגנטי

השתמשנו ב $muSR$ בכדי למדוד את פרמטר הסדר האנטיפרומגנטי בטמפרטורת הבסיס

M_0, כתלות בסימום החורים הנמדדת מסימום אופטימלי Δp_m. המדידות התבצעו עבור במערכת העל מוליכים: $(Ca_xLa_{1-x})(Ba_{1.75-x}La_{0.25+x})Cu_3O_y(CLBLCO)$. כל x שונה מהווה משפחה שונה של על מוליכים. במערכת זו T_C המכסימלי ופרמטר הצימוד המגנטי J משתנים ב 30% בין המשפחות. מצאנו כי התלות של M_0 ב Δp_m אינה תלויה במשפחה.

בנוסף לכך ביצענו מדידות של פיזור נויטרונים על מנת למדוד את פרמטרי השריג כתלות במשפחה וברמת הסימום. מתוך מדידות אלו, ותוך שימוש בשיקולים מבניים של השריג ניתן להעריך את הפרמטר הצימוד המגנט J ואת קצב הדילוג t של מודל ה $t-J$. הראנו כי המקור העיקרי לשינוי בטמפרטורת המעבר העל מוליכה המכסימלית בין המשפחות היא זווית הכיפוף בין החמצן לנחושת במישורים. השוואה בין היחס t/J, כפי שחולץ מתוך מדידת פיזור הנויטרונים, והתלות של M_0 ב Δp_m, מלמדת כי עבור תרכובת זו פרמטר הסדר כתלות במספר החורים אינה תלויה ה t/J, בניגוד למצופה ממודל t/J.

אנו מציעים מספר הסברים אפשריים לתוצאות אלה. אפשרות אחת היא שבטמפרטורות נמוכות ההמילטוניאן האפקטיבי נתון ע"י מודל ה $t-J$, אבל בעל t שהוא פרופורציונאלי ל J. אפשרות נוספת היא שההרס של פרמטר הסדר המגנטי הוא לא תוצאה של קפיצה של חורים בודדים על רקע אנטיפרומגנטי, ויש צורך לתאר את המערכת עם המילטוניאן שונה, אולי כזה המתאר קפיצה של זוגות בוזונים.